Applied Surface Science 528 (2020) 146952

Contents lists available at ScienceDirect

Applied Surface Science

journal homepage: www.elsevier.com/locate/apsusc

Two-level ablation and damage morphology of Ru films under femtosecond extreme UV irradiation

I. Milov[a,*], V. Zhakhovsky[b,c], D. Ilnitsky[b], K. Migdal[b], V. Khokhlov[d], Yu. Petrov[d,e], N. Inogamov[c,d], V. Lipp[f], N. Medvedev[g,h], B. Ziaja[f,i], V. Medvedev[e,j], I.A. Makhotkin[a], E. Louis[a], F. Bijkerk[a]

[a] Industrial Focus Group XUV Optics, MESA+ Institute for Nanotechnology, University of Twente, Drienerlolaan 5, 7522 NB Enschede, The Netherlands
[b] Dukhov Research Institute of Automatics, Sushchevskaya 22, Moscow 127055, Russia
[c] Joint Institute for High Temperatures, Russian Academy of Sciences, Izhorskaya st. 13 Bd.2, Moscow 125412, Russia
[d] Landau Institute for Theoretical Physics, Russian Academy of Sciences, Chernogolovka 142432, Russia
[e] Moscow Institute of Physics and Technology, Institutskiy per. 9, 141701 Dolgoprudny, Moscow Region, Russia
[f] Center for Free-Electron Laser Science CFEL, Deutsches Elektronen-Synchrotron DESY, Notkestrasse 85, 22607 Hamburg, Germany
[g] Institute of Physics, Czech Academy of Sciences, Na Slovance 2, 182 21 Prague 8, Czech Republic
[h] Institute of Plasma Physics, Czech Academy of Sciences, Za Slovankou 3, 182 00 Prague 8, Czech Republic
[i] Institute of Nuclear Physics, Polish Academy of Sciences, Radzikowskiego 152, 31-342 Krakow, Poland
[j] Institute for Spectroscopy, RAS, Fizicheskaya st. 5, Troitsk, Moscow Region, Russia

A R T I C L E I N F O

Keywords:
Femtosecond laser ablation
Free-electron laser
Extreme ultraviolet
Molecular dynamics
Monte Carlo
Thin films

A B S T R A C T

The dynamics of a thin ruthenium film irradiated by femtosecond extreme UV laser pulses is studied with a hybrid computational approach, which includes Monte Carlo, two-temperature hydrodynamics and molecular dynamics models. This approach is capable of accurate simulations of all stages of material evolution induced by extreme UV or X-ray photons: from nonequilibrium electron kinetics till complete lattice relaxation. We found that fast energy deposition in a subsurface layer leads to a two-level ablation: the top thin layer is ablated as a gas–liquid mixture due to expansion of overheated material at near and above critical conditions, whereas a thicker liquid layer below is ablated via a cavitation process. The latter occurs due to a thermo-mechanically induced tensile pressure wave. The liquid ablating layer exhibits unstable behaviour and disintegrates into droplets soon after detachment from the rest of the target. Our simulations reveal basic processes leading to formation of specific surface morphologies outside and inside the damage craters. The calculated ablation threshold, crater depth and morphological features are in quantitative agreement with the experimental data, which justifies the applicability of our hybrid model to study laser-induced material damage.

1. Introduction

The rapid development of free electron lasers (FELs) leads to a continuous increase of the pulse intensity at such facilities. Recent reports claim the achievement of sub-micron focusing of the light down to a 50 nm spot size, which will result in an on-target peak intensity above 10^{20} W/cm^2 [1,2]. Such an extreme intensity can transfer irradiated materials into highly excited non-equilibrium states that are still not fully understood [3]. Apart from the target itself, the optical elements at the FEL facilities can be illuminated with high radiation doses as well, which can lead to irreversible changes and degrade their performance. Numerous experimental studies of damage of the materials relevant to the extreme ultraviolet (XUV) and X-ray optics were performed to determine failure conditions of the optical elements [4–14].

One of the common damage mechanisms occurring after irradiating matter with ultrashort pulses of moderate to high intensity is laser ablation [15]. Apart from the fundamental interest in the context of warm dense matter studies [3,16–18], the phenomenon of laser ablation has been widely utilized in many applications such as pulsed laser deposition [19], laser-induced breakdown spectroscopy [20], laser propulsion [21], laser printing [22], surface micromachining [23] and nanoparticles production [24]. The latter includes applications in plasmonics [25], catalysis [26] and biomedicine [27].

Different applications of laser ablation require a different final outcome of the ablation process, for example, different size, shape and structure of the produced nanoparticles, or different morphology of the

---

* Corresponding author.
E-mail address: i.milov@utwente.nl (I. Milov).

https://doi.org/10.1016/j.apsusc.2020.146952
Received 12 February 2020; Received in revised form 28 May 2020; Accepted 9 June 2020

surface nanostructures. Such a sensitive control of the ablation process can only be achieved if all physical mechanisms involved in the interaction of high intensity ultrashort laser pulses with matter are quantitatively understood. For that, the dedicated experimental studies should be supplemented with reliable computational models.

The complex nature of light-matter interaction involves various physical processes occurring on a broad temporal scale. In order to describe the full timescale of material evolution under laser irradiation, from the initial excitation to the final material removal during the ablation process and relaxation of the irradiated target, one typically has to apply hybrid computational schemes. Hybrid simulation techniques combine several models into a unified approach to efficiently describe various sub-problems within the complex problem studied. They include, for example, multiscale techniques [28,29], and similar approaches [30].

Combinations of the two-temperature-based models (TTM [31–33] or two-temperature hydrodynamics [34]) with the molecular dynamics (MD) method are commonly used to describe ultrafast laser ablation of metals [35–38]. For semiconductors, a modification of the classical two-temperature model has been applied to take into account the non-constant density of conduction band electrons and valence band holes [39,40]. The combination of such a density dependent TTM with the MD was used to study the interaction of femtosecond laser pulses with Si targets [41,42]. Another approach which combines a Monte Carlo (MC) method with MD was applied to simulate melting, ablation, and solidification in Si induced by laser pulses with different duration [43].

Hybrid schemes that include two-temperature-based parts usually consider the electronic system to always be in a thermodynamic equilibrium, so that it can be described with an electronic temperature. In case of metals, such an approximation is typically valid if the photon energy is low (infrared and optical range), so that only the conduction band electrons are excited, and their thermalization is fast (on the femtosecond timescale). However, it was experimentally shown [44,45] and theoretically verified [46,47] that the electron gas in a metal excited with an optical or infrared femtosecond lasers can stay out of equilibrium for a few hundred fs up to the picosecond timescale. Such behaviour of the excited electronic system can limit the applicability of the two-temperature-based models to timescales above ~1 ps only. In order to overcome this limitation, a full Boltzmann collision integral approach can be used to investigate a transient evolution of a non-equilibrium electron distribution function [48], which demonstrates that, generally, equilibration within the electronic system of a metal occurs faster when increasing the fluence of a femtosecond optical pulse.

Absorption of higher energy XUV or X-ray photons (~10 eV and higher) results in a non-equilibrium electron kinetics that cannot be neglected. The X-ray induced electron cascades in matter can be efficiently simulated with Monte-Carlo-based (MC) models [49–51].

To have a more complete understanding of how X-ray irradiated materials evolve, including both electronic and atomic systems, one may use hybrid approaches. For instance, in the work [52] the authors used the X-RIM code to model the X-ray FEL (XFEL) interaction with ruthenium and silicon at the damage threshold intensity. The code links the calculations of the radiation field in the material with the hydrodynamics (HD) simulations. One should note that the HD part of the model limits it to the elastoplastic regime only. As another example, a hybrid approach XTANT (X-ray-induced Thermal And Non-thermal Transition) [30] simulates material evolution taking into account non-equilibrium electron distribution, non-adiabatic electron–ion energy exchange, transient electron band structure, atomic potential energy surface evolution, and atomic motion, within one interconnected model. The complexity of parallel calculations of various physical processes restricts the model to a timescale up to ~100 ps and system size up to ~1000 atoms.

In our previous work [53], focused on the effect of different energy of the incident photons on the early stage of ruthenium (Ru) target evolution, we reported on our combined MC–HD approach. This approach was capable of reliable simulations of material evolution only during the early picosecond stage after irradiation, but was not able to simulate significant lattice modifications on a longer timescale. A combination of HD with MD was also developed previously (see Ref. [34] for example), but it did not take into account nonequilibrium electron kinetics, hence was not applicable in case of photon energies sufficiently high to induce electron cascades.

In this work, to overcome these limitations and to cover all stages of material response to irradiation, we combine the mentioned approaches together. Thus, a new hybrid model with a significantly extended applicability is implemented, which is a combination of Monte Carlo, hydrodynamics and molecular dynamics. This model simulates the material evolution from photoabsorption (∼100 fs) to complete relaxation and formation of the final damage morphologies (∼1–10 ns). The in–house parallel MD code with the highly adaptive load balancing algorithm [54,55] allows to consider large systems with a highly non-uniform mass distribution and a number of atoms above 10^8.

The model is applicable in a wide range of photon energies from XUV to hard X-rays. An extension down to optical or NIR photon energies is possible with a replacement of the MC module with a TTM-based approach if applicable, or with a Boltzmann kinetic equation in a general case. The applicability of the MC–HD part of the model in the case of 800 nm laser light was demonstrated in [53]. Any metal can be considered if the required parameters that describe the physical properties of a metal in the one- and two-temperature states are known.

We apply our model to study the dynamics of a Ru thin film under femtosecond extreme UV laser irradiation in the intensity regime below and above the ablation threshold. Ru is chosen as a material that can be used as a grazing incidence mirror in the XUV and hard X-ray regimes [8,9,11]. We focus on the atomistic picture of material evolution, because it provides us with the detailed understanding of physical processes responsible for material damage, and gives us access to the direct comparison of simulation results with the experiment. The specific irradiation conditions that we use to verify our model are dictated by the single-shot damage experiment performed at the femtosecond XUV free-electron laser in Hamburg (FLASH [56]) that was reported in Refs. [11,57].

The parameterization of the model to be applied for a particular material (Ru in our case) is based on reproducing the known mechanical and thermophysical properties of the material, as will be discussed below in detail. No knowledge of the results of the light-matter interaction experiments is required as input data. Therefore, our model can be used not only to describe the existing experiments, but also to predict the results of the future ones.

2. Hybrid computational model

The femtosecond duration of the laser pulses allows one to separate the physical processes involved in the light-metal interaction in time [58]. Three characteristic stages can be identified. (i) Absorption of light and the following non-equilibrium electron kinetics. During that stage, if the photon energy is sufficiently high, photo- and secondary electrons created upon photoabsorption propagate in a metal and create electron cascades [50]. The cascading process depends on the photon energy and material properties and continues until all excited electrons become slow and can be considered as thermalized in the conduction band [53]. At the end of this stage electrons are at high temperature, while ions are still cold. (ii) Two-temperature (2T) state of the irradiated metal. At this stage the target can be represented as consisting of electronic and ionic subsystems, both in local thermal equilibrium, with the corresponding individual temperatures T_e and T_i. The 2T stage lasts as long as T_e is considerably different from T_i. During that stage, the absorbed laser energy, stored in the thermalized electrons, diffuses into the depth of the material, while simultaneously interacting with the ionic subsystem, which results in heating of the latter. If the characteristic heating time is faster than the time required for a material to

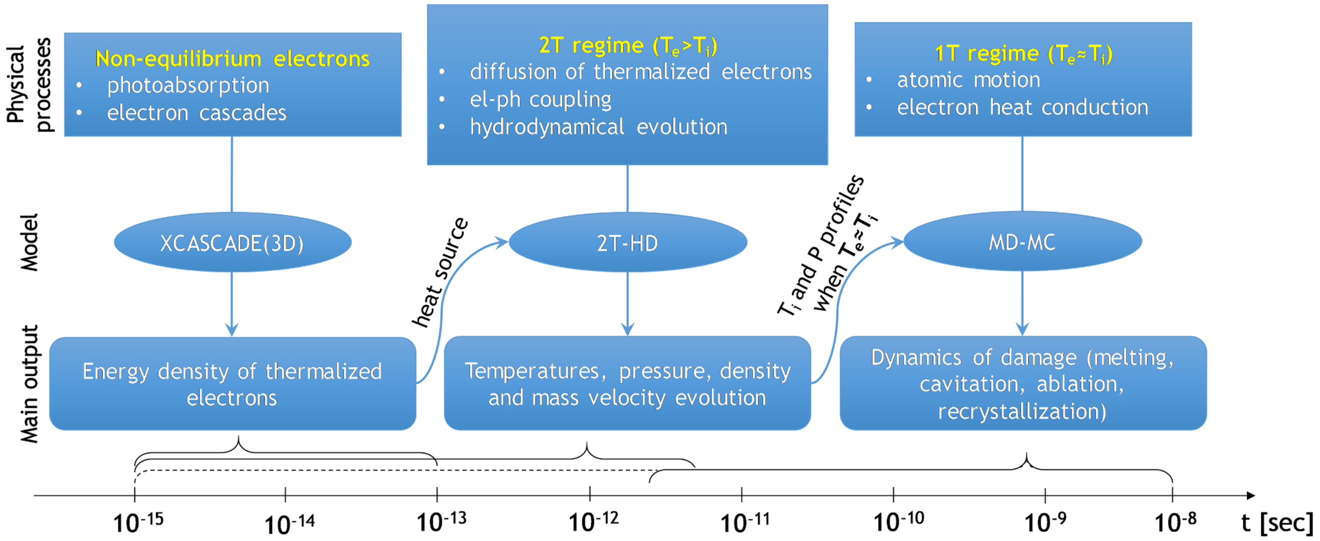

Fig. 1. Basic processes and corresponding simulation techniques used in our hybrid model.

mechanically react to it by expanding, the heating is effectively isochoric. This situation is usually referred to as stress confinement regime [36,59]. As a result, thermo-induced stresses are generated. (iii) The 2T stage proceeds into the one-temperature (1T) stage after thermal equilibrium between electrons and ions is reached ($T_e \approx T_i$). The evolution of the material, started in the 2T stage, continues. If the laser fluence is sufficiently high, such evolution typically includes melting, cavitation, ablation and recrystallization processes. Electrostatic processes such as Coulomb explosion are unlikely to occur in metals at moderate fluences [60] and therefore are not considered in this work.

Developing a model to describe laser pulse interaction with a metal, we exploit the time separation of the whole process into three distinct stages, determined by fast electron response to an ultrashort laser pulse irradiation, then by electron diffusion and electron-ion energy exchange, and finally by slow evolution of the ionic system, respectively. We use three different models, one for each stage, and combine them into one hybrid approach. Due to the femtosecond duration of the laser pulse, it is possible to model the physical processes at each stage sequentially [58]. The model scheme is presented in Fig. 1 and will be described below in more detail.

2.1. XCASCADE(3D)

The photoabsorption and the following non-equilibrium electron kinetics are modeled with the asymptotic trajectory classical MC code XCASCADE(3D) [51]. The target is represented as a homogeneous arrangement of atoms with a density corresponding to the chosen material. The photoabsorption cross sections, electron scattering cross sections and the ionization potentials of the target, taken from the EPICS2017 databases [61], are described in the atomic approximation.

The MC code accounts for the following processes: photoabsorption by valence and core–shell electrons, Auger recombination of created deep holes with release of Auger electrons, propagation of photo- and secondary electrons, and both inelastic (impact ionization) and elastic scattering of electrons on neutral atoms. All photo- as well as secondary electrons are traced until their energy falls below a predefined cutoff energy. Electrons with energies below this cutoff, as well as holes created in the valence atomic levels, are considered as thermalized electrons in the conduction band of the metal. The spatio-temporal energy density of these thermalized electrons forms a heat source for the two-temperature hydrodynamics (2T-HD) code [53].

As it was shown in previous studies, an electronic system of a solid under femtosecond XFEL irradiation follows the so called “bump-on–hot-tail” distribution [62,63]: the majority of low-energy electrons is almost in thermal equilibrium, with the minority of the highly excited electrons forming the high-energy out-of-equilibrium tail of the distribution. In our approach, the nonequilibrium cascading of high-energy electrons is modeled with the XCASCADE(3D) code, whereas the low-energy (thermalized) electrons are treated with the 2T-HD code. A possible deviation of the low-energy electrons from the Fermi–Dirac distribution is not taken into account. This would require dedicated simulations with, e.g., the Boltzmann equation [48]. It is expected that within the bump-on–hot-tail distribution, such deviations are small [63].

The applicability of the XCASCADE(3D) code is limited to the fluence regime when the density of cascading electrons is considerably lower than the atomic density. In that case, the electron-atom scattering is dominant, while scattering among excited electrons can be neglected. We checked that this condition was fulfilled for all the fluences considered in this work: the electron density does not exceed 1% of the atomic density. There are no plasma effects at the level of excitation considered here. All electron cascades evolve in solid state Ru, and they finish long before any phase transition occurs.

An *a posteriori* analysis of our results suggests that during the cascading time, the irradiated material properties used in the XCASCADE (3D) simulations do not significantly change. That justifies a coupling between XCASCADE(3D) and 2T-HD within a scheme without feedback, when the output data from the MC simulations are passed one-way into the 2T-HD model as the input (source term), see Fig. 1. Therefore, the XCASCADE(3D) code can be applied to model the cascading processes in the irradiated target even at high fluences at which structural damage is expected on a later timescale, if the cascading time is sufficiently short.

2.2. Two-temperature hydrodynamics and equation of state

The hydrodynamic behaviour of the material in the 2T stage is modeled with our Lagrangian 2T-HD code [34,53]. The code simulates the evolution of material properties, namely density, pressure, mass velocity, and electron and ion temperatures, induced by the heat source obtained with the XCASCADE(3D) calculations.

The 2T equations of state that govern the thermodynamics of Ru, together with the 2T thermal conductivity and the electron–phonon coupling factor, are taken from our previous work [64], where these properties were obtained from *ab initio* calculations. The equations of state are currently obtained only for the solid phase of Ru, which means that melting and evaporation are not taken into account in the 2T stage. These processes are naturally described with the MD code, although we cannot guarantee completely reliable simulation of them during the 2T stage. However, this stage in Ru lasts for a relatively short time (2–3 ps), ending before significant melting and material ejection occur, so the possible inaccuracy in the description of the 2T stage is insignificant. More details on that are described in Section 3.2.

We include electron pressure P_e into the 2T-HD code. The total pressure $P = P_i + P_e$ is responsible for material movement. At the border with vacuum, according to our boundary conditions the total pressure is always zero, so $P_e = -P_i$ at the Ru-vacuum interface. This means that the outermost Lagrangian particle (LP) at any moment of time has to adjust so that this boundary conditions is fulfilled. Typically, the outermost LP stretches significantly into vacuum to guarantee zero total pressure at the boundary. Such a boundary condition is realistic at moderate fluences, when the formation of dense plasma and vapour can be neglected during the time when the electron pressure is strong.

We carry out the 2T-HD calculations until the end of the 2T stage when the thermal equilibrium between the electronic and ionic systems is reached: $T_e \approx T_i$ within the entire Ru thickness. The total pressure and the ion temperature depth profiles at the end of the 2T-HD simulation are stored. After that, we run the MD code starting again from the absorption of a laser pulse. The initial conditions of the MD code and the parameters simulating Monte Carlo pseudo-electrons (MD-MC approach [54]) are adjusted to reproduce the stored hydrodynamic profiles at the end of the 2T stage. With such a scheme, we guarantee that with the MD simulations we arrive at the correct state of excited material predicted with the 2T-HD. Synchronized with the 2T-HD after the electron–ion equilibration is reached, the MD-MC code continues alone and describes further material evolution until complete relaxation. The details of this scheme applied to Ru are described in Section 3.2 and Appendix A.

The subsequent material evolution in the 1T regime is modeled with our classical MD code that simulates atomic motion, while the electronic heat conductivity is taken into account within the Monte Carlo formalism (MD-MC approach) [54].

2.3. Molecular dynamics combined with MC electrons

Material evolution in the 1T state is modeled with the classical MD method [54,55]. Classical MD by default takes into account only the atomic system, whereas free electrons are not considered. Electron heat conductivity plays a very important role in the context of laser damage of metals, and thus has to be included into the model. Combination of continuous TTM with MD is one of the ways to do that [35]. In our work we use a different approach to include electron heat conductivity into the classical MD scheme, namely the MC method described in detail in Ref. [65].

Instead of real quantum electrons we introduce classical pseudo-particles with a mass not related to the effective electron mass in the material. These particles can ‘hop’ between moving neighbouring atoms, whose motion is simulated with the MD method. For simplicity, we will refer to these particles as ’pseudo-electrons’, although they are not real electrons and are introduced solely as a method to solve heat transfer in a complex 3D geometry of the evolving target. Each host atom has one MC pseudo-electron, which has its own momentum, but its position is always allocated on its host atom. It guarantees the charge neutrality in the combined electron-atom system at any conditions, simplifying the simulations. A randomly chosen pair of pseudo-electrons allocated at neighbouring atoms swaps over their hosts with a certain rate, which is a free MC parameter that has to be defined in order to reproduce the experimental thermal conductivity. Such swapping of pseudo-electron momenta results in a diffusion of thermal energy on a mobile atomic network, which can reproduce heat conduction in a moving material having a complex geometry with voids. After each hop, a pseudo-electron exchanges energy with its new host atom via a collision, enabling electron-atom energy coupling.

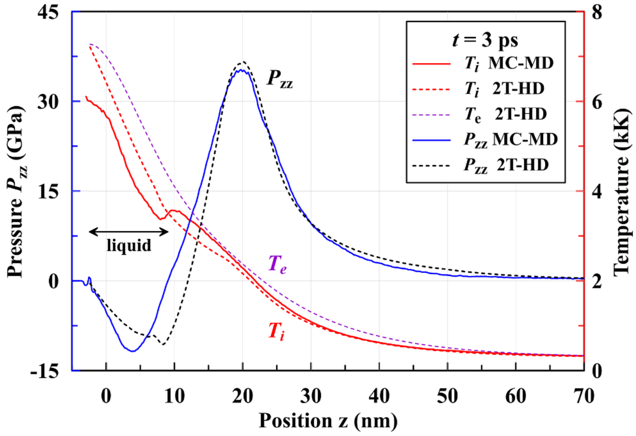

Fig. 2. Comparison of temperature and pressure profiles calculated with the 2T-HD and the MD-MC methods, which illustrates the procedure of linking these two methods in our hybrid scheme. The absorbed fluence is $F_{abs} = 40$ mJ/cm^2.

Our MC model is parameterized with two fitting parameters: the mass of pseudo-electrons and the exchange rate. The latter is used for both swapping and electron–ion collision rates. The details of the parametrization procedure are described in the Appendix A.

To reliably simulate the atomic motion, one has to use the MD interatomic potential most suitable for the problem under investigation. In the context of light-matter interaction at high intensities, the interatomic potential must properly reproduce the material properties at extreme conditions, namely at high temperatures and under strong pressures. For that purpose, we developed the Ru interatomic potential in the framework of the embedded atom model (EAM) using the stress-matching method [66,67]. The procedure is described in Appendix B, and the interatomic potential itself is available in the Supplementary Material.

Post-mortem analysis of the experimental ablation craters in the Ru/Si target showed that the damage is confined to the Ru layer, with no visible damage to the Si substrate at the studied fluences [57]. To avoid unnecessary difficulties when using separate interatomic potentials for Si atoms and for Ru-Si interaction at the interface, we model the Si substrate with a layer composed of Ru pseudo-atoms, which are arranged in the same crystal structure as the original Ru film. The mass of the Ru pseudo-atoms is modified to reproduce the acoustic impedance of the Si substrate. This technique provides a correct description of the pressure wave reflection from the Ru-substrate interface (the mechanical properties of Si are reproduced), although the thermal properties of our model Si, which we will refer to as a “substrate”, should be adjusted separately. A similar approach was successfully used to model the Ni-on-glass system [68]. The correct thermal conductivity in the substrate is achieved by adjusting the MC pseudo-electron exchange rate parameter in the MD box region that corresponds to the substrate.

The effect of thermal boundary resistance of the Ru-substrate interface was tested by changing the probability of MC pseudo-electrons exchange through the interface. We found no significant effect of the heat transfer through the interface on the dynamics of material evolution.

The MD-MC calculations are performed for a system of 50 nm thick hexagonal close-packed (*hcp*) Ru on a substrate, composed of Ru pseudo-atoms. The periodic boundary conditions are applied in two lateral directions (x and y). The in-depth size L_z of the MD simulation box is taken to be 150 nm (50 nm Ru and 100 nm substrate). Non-reflecting boundary conditions at the bottom of the substrate are applied, which means that the pressure wave that arrives at the bottom of the simulation box is completely absorbed by the boundary to mimic bulk material.

The following additional procedure is introduced in order to accurately simulate the thermal conductivity in the finite size substrate. First, we perform a calculation with a simulation box of small lateral sizes L_x and L_y and large in-depth size L_z: $8 \times 8 \times 650\ \mathrm{nm}^3$. The periodic boundary conditions are applied in x and y lateral directions. The velocity $u(t)$ and temperature $T(t)$ history of a Lagrangian particle (LP) in the layer $150 - 152$ nm is recorded. After that, we perform a new calculation with an $8 \times 8 \times 150\ \mathrm{nm}^3$ box, where the LP history from the previous step is used for the bottom boundary. We check that the temperature and pressure depth profiles in the top 150 nm are the same in these two calculations. Finally, a calculation with desired L_x and L_y and with $L_z = 150$ nm is performed using the LP time history. With such an approach we ensure that we can mimic a thick Si substrate. Not only the pressure wave is absorbed at the bottom of the simulation box, but also the thermal conductivity in a large system ($L_z = 650$ nm) is properly reproduced using a smaller system ($L_z = 150$ nm).

3. Simulation results

3.1. Non-equilibrium electron kinetics

We performed simulations of XUV (92 eV or 13.5 nm), 100 fs FWHM laser pulses interaction with the Ru-on-substrate target using our hybrid model. We considered grazing incidence of the XUV pulses (20° with respect to the surface), since this condition was used in the experiment [57] that we aim to compare our results with, see Section 4. The corresponding photon penetration depth is 3.5 nm, and the surface reflectivity is 68%.

First, the photoabsorption and the electron cascades kinetics are simulated with the XCASCADE(3D) code. In previous papers [53,57,69] we studied the spatio-temporal characteristics of electrons in XUV-irradiated Ru at the ablation threshold fluence. In particular, it was shown, that the cascading process in Ru induced by 92 eV photons was extremely fast (<1 fs) and the cascading electrons on average travel a very short distance of about $1 - 2$ nm before the thermalization, see Figs. 5 and 6 in Ref. [57]. The amount of energy that escapes from the surface via photo- and secondary electrons was calculated to be ~9%. Therefore, the cascading process in the 92 eV case is not significant, although for higher photon energies the non-equilibrium electrons can play a crucial role in the damage processes [53].

3.2. Two-temperature hydrodynamic evolution

The 2T evolution of Ru is simulated with our 2T-HD code. We run the 2T-HD code until the end of the 2T stage when the thermal equilibrium between electrons and ions is reached. After that, the MD-MC simulation takes over, ensured that its state at the end of the 2T stage corresponds to the state predicted with the 2T-HD. Adjusting the MD-MC parameters it is crucial to reproduce the *shape* of the 2T-HD profiles. The amplitudes of the profiles are determined by the absorbed fluence.

In general, the procedure of adjusting the initial conditions and the MC parameters (see A) of the MD-MC code to match the output of the 2T-HD should be performed for all considered fluences. However, in the case of Ru, the shape of the 2T-HD profiles weakly depends on fluence. This is due to the fact that the thermal diffusivity k_e/C_e of Ru is almost constant at high electron temperatures (electron thermal conductivity k_e and heat capacity C_e both linearly increase with electron temperature in high temperature region, see Ref. [64]). Additionally, the electron-phonon coupling factor weakly depends on electron temperature [64].

The weak dependence of the shape of the 2T-HD profiles on fluence is also supported by the experiment, where the crater depth (which is connected to the heat affected zone and pressure profile) is constant in a large central region of the damage crater (see Fig. 12 below). This fact allows us to perform the procedure of fitting the shape of the MD-MC temperature and pressure profiles to the 2T-HD ones only once. Obtained for one fluence, the same parameters are used for all MD-MC calculations in this work. To minimize the effect of melting, which is not taken into account in the 2T-HD code, we use the lowest considered fluence of $F_{\mathrm{abs}} = 40\ \mathrm{mJ/cm^2}$ for the fitting procedure. The time $\tau = 3$ ps, when the two codes are linked, is chosen as the time when thermal equilibrium is reached, $T_e(z) \approx T_i(z)$.

The 2T-HD profiles $T_i(z)$ and $P_{zz}(z)$ at $t = 3$ ps are shown in Fig. 2, where they are compared with the same profiles obtained with the MD-MC code. The 2T-HD electronic and ionic temperature profiles are close to each other along the entire Ru thickness, which demonstrates the

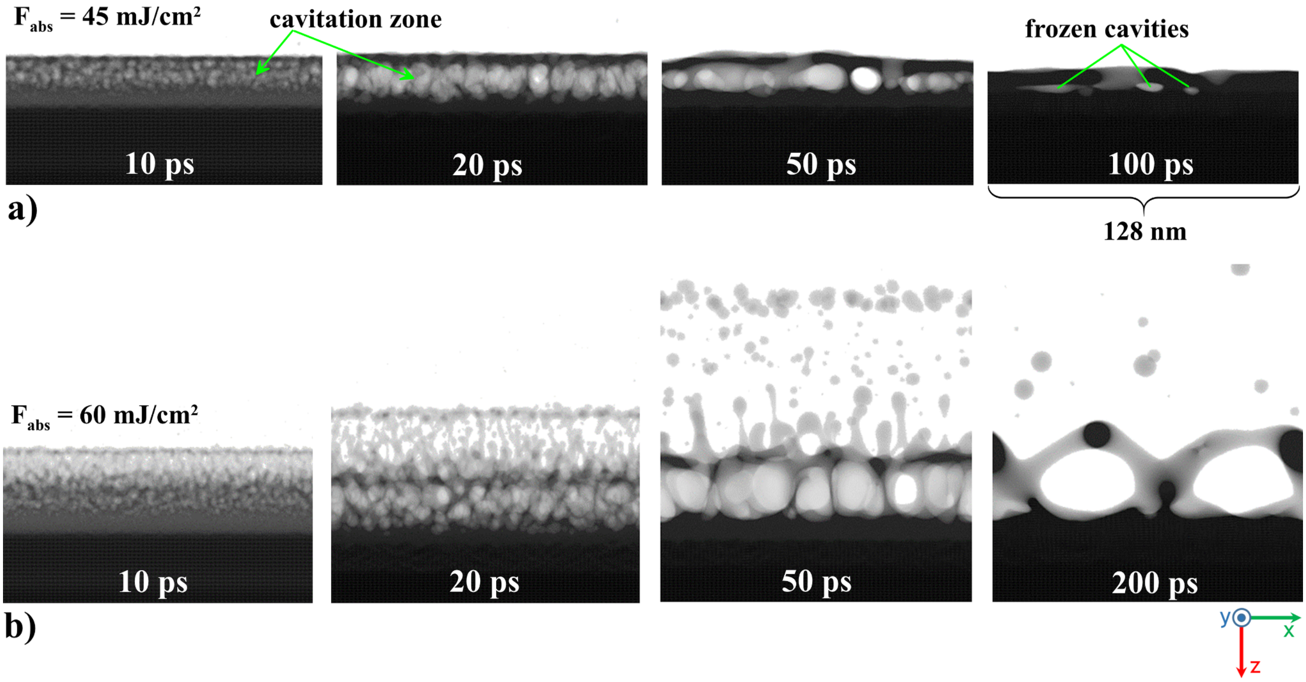

Fig. 3. Mass distributions obtained with the MD-MC calculations. The evolution of the Ru-on-substrate target irradiated with a 100 fs XUV laser pulse is shown for the absorbed fluences of (a) $F_{\mathrm{abs}} = 45\ \mathrm{mJ/cm^2}$ and (b) $F_{\mathrm{abs}} = 60\ \mathrm{mJ/cm^2}$. Only the top parts of Ru that are subjected to structural modifications are shown.

establishment of thermal equilibrium. In the fitting procedure of the MD-MC profiles to the 2T-HD ones, we used only the region $z \geq 10$ nm. That is because the top part of Ru $z < 10$ nm is considered as molten: $T_i > T_m + T_h$ in that region, $T_h = H_m/C_i = 746$ K. Here $H_m = 4.7 \cdot 10^9$ J/m^3 is the latent heat of melting and $C_i = 6.3 \cdot 10^6$ J/m^3/K is the ion heat capacity at the melting temperature [70]. Since melting is not included in the 2T-HD, the temperature and pressure profiles in the liquid region may contain inaccuracies, therefore we do not use this region in the fitting procedure.

There is a good agreement between the 2T-HD and the MD-MC profiles in the region $z \geq 15$ nm. The difference in the top region $z < 15$ nm can be due to the following reasons. As just mentioned above, melting is not taken into account in the 2T-HD, but is naturally included in the MD-MC code. It is known, that melting can influence the amplitude of the pressure wave, but as one can see, this effect is small in Ru. The speed of sound is higher in the solid phase, which can explain the deeper position of the 2T-HD pressure minimum compared to the MD-MC one. Another reason for the different positions of the pressure minima can be due to the electron pressure, which is taken into account in the 2T-HD, but is not included in the MD-MC calculations. The existence of a strong electron pressure in the 2T-HD approach due to the high electron temperature during the first $1 - 2$ ps can result in the formation of a tensile wave (negative pressure) sooner than in the MD-MC code.

Overall, the difference between the 2T-HD and the MD-MC profiles is small, which demonstrates a successful linking of the two codes. A possible inaccuracy, resulting from the fact that (i) phase transitions are not included into the 2T-HD code and (ii) electronic pressure is not included into the MD-MC code, is minimized with our fitting procedure; so it should not affect the following long-time scale material evolution that we focus on in this work.

The XCASCADE(3D) and 2T-HD calculations at the ablation threshold are used to tune the parameters of the MD-MC code, so that with the MD-MC calculations we enter the 1T stage of material evolution in a correct way.

Below we present the results of a series of MD-MC calculations for different fluences in the pre- and above ablation regimes in order to study the evolution of the Ru target on an atomistic level. We aim to identify and describe the physical processes responsible for different regimes of Ru laser-induced damage.

3.3. *Fluence dependent atomistic picture of material evolution*

In this section we report the results of our MD-MC simulations on the dynamics of a 50 nm Ru film exposed to single 100 fs FWHM XUV laser pulses of various fluences. The size of the MD box used is $128 \times 32 \times 150$ nm^3. It contains ~46 million atoms. The lateral dimensions 128×32 nm^2 are chosen to be sufficiently large, so that the maximum size of the features that we obtain in our simulations for all considered fluences is smaller than the size of the box. The procedure of mimicking a thick Si substrate in the depth direction (via Ru pseudo-atoms) was described above. The periodic boundary conditions are applied in x and y lateral directions. Each simulation is performed with a top-hat shape of the laser pulse.

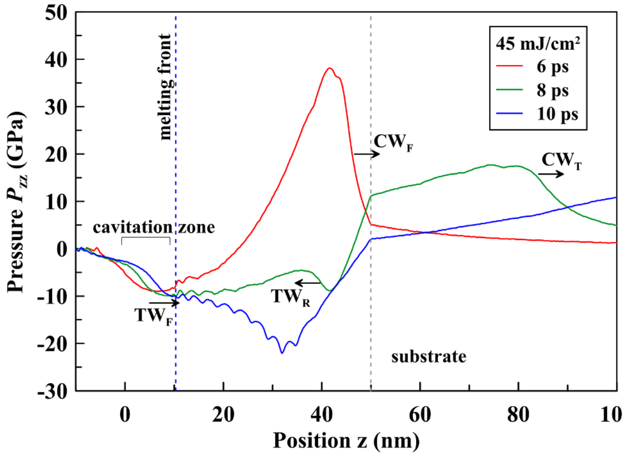

Fig. 4. Evolution of pressure in the Ru-on-substrate target irradiated with a 100 fs XUV laser pulse. The absorbed fluence is $F_{abs} = 45$ mJ/cm^2. The blue dashed line indicates the position of the melting front at $t = 10$ ps.

We start with a relatively low absorbed fluence of 45 mJ/cm^2. The corresponding mass distributions at different times are shown in Fig. 3 (a). The laser pulse comes from the top. The time $t = 0.5$ ps corresponds to the moment when the maximum intensity of the laser pulse is at the Ru surface.

The transfer of the absorbed energy from the electronic system to the lattice results in ultrafast melting of the top Ru layer. The maximum molten depth of 14 nm is reached at $t = 20$ ps. The ultrafast heating in the stress-confinement regime induces a strong compressive pressure wave at the front Ru surface. The time evolution of the thermo-induced pressure wave is shown in Fig. 4. The frontal compressive wave CW_F propagates into the depth of the target and is followed by a tensile wave TW_F. It propagates in the molten Ru with an increasing amplitude. A rupture occurs when the amplitude of this tensile wave is sufficient to overcome the tensile strength of the material. Comparing the mass distributions with the pressure profiles, one can see that a cavitation zone is created in liquid Ru as a result of propagation of the frontal tensile wave TW_F. The cavitation threshold, i.e. the minimum fluence required to produce a cavity, is found with separate MD-MC calculations to be ~30 mJ/cm^2.

When the compressive wave CW_F reaches the Ru-substrate interface, it is partially transmitted through the interface (CW_T wave) and is partially reflected back with a change of sign (TW_R wave), see Fig. 4. Although large in amplitude, this reflected wave does not cause damage, as one can see from the mass distributions in Fig. 3 (a), since it propagates in the solid material, which has a higher strength than a liquid. There is no experimental data on the tensile strength of Ru at high strain rates, but our simulations indicate that it is above 20 GPa for solid Ru. The tensile strength of liquid Ru can be estimated from the pressure profiles in Fig. 4 and is about $5 - 10$ GPa at a temperature of ~5000 K and a strain rate ~$8 \cdot 10^{10}$ 1/s. Identification of the exact value of the tensile strength is beyond the scope of the present work, since it is difficult to trace at which conditions the first cavity is formed.

One can see from the mass distributions in Fig. 3 (a) that the fluence of 45 mJ/cm^2 is not sufficient to cause ablation. The cavitation zone collapses due to the surface tension, which is strong in Ru (see Ref. [71] and Appendix B). The resolidification front that arrives from the depth freezes the target with small subsurface cavities at about 160 ps.

Fig. 3 (b) shows simulation results at the absorbed fluence of 60 mJ/cm^2. Unlike the previous case, ablation of the top thin layer of Ru is observed. It is important to note that ablation starts at the fluence twice higher than the cavitation threshold (see Discussion 5). The higher fluence creates a stronger pressure gradient and, hence, higher velocity of the top liquid layer – sufficient to cause ablation. Another factor in favour of ablation is a higher temperature of the top layer, which reduces the tensile strength. The propagation of the tensile wave into the depth causes a cavitation zone below the ablated thin layer. The produced cavities emerge during the stretching of the cavitation zone. At a time of about 200 ps only two large cavities remain and start to collapse (not shown).

Ablation of a larger amount of material occurs at higher fluences, as shown with the mass distributions in Fig. 5. At 90 mJ/cm^2 the early stage of material evolution is similar to the previous case of 60 mJ/cm^2: ablation of the top thin layer and the formation and stretching of the cavitation zone below. The difference to the previous case is that now the cavitation zone does not collapse, but is stretched significantly until the binding material between the ablating layer and the remaining

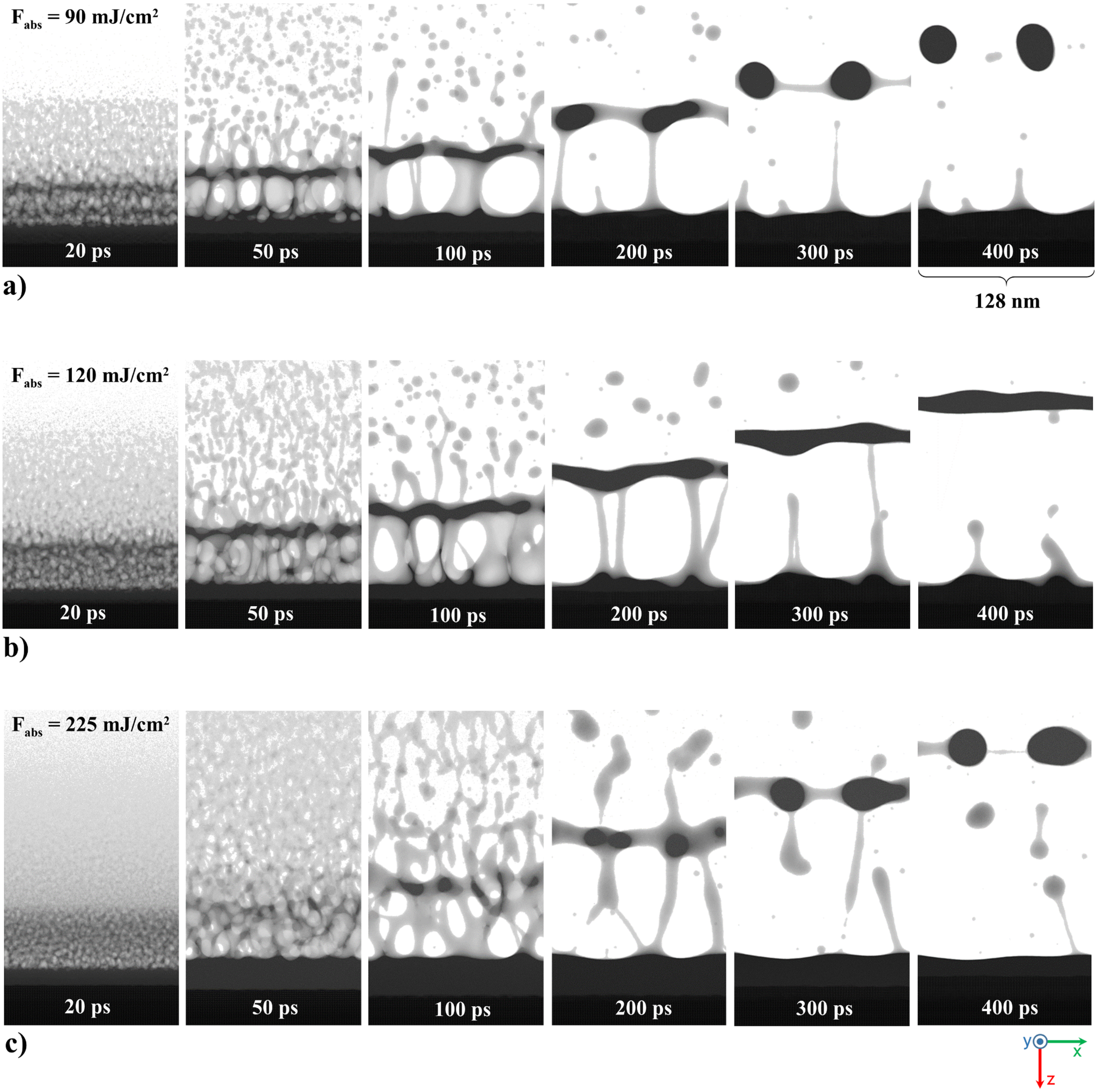

Fig. 5. Mass distributions obtained with the MD-MC calculations. Evolution of the Ru-on-substrate target irradiated with a 100 fs XUV laser pulse is shown for the absorbed fluences of (a) F_{abs} = 90 mJ/cm^2, (b) F_{abs} = 120 mJ/cm^2 and (c) F_{abs} = 225 mJ/cm^2. Only the top parts of Ru that are subjected to structural modifications are shown. Movies of mass distribution and symmetry parameter evolution from these simulations can be found in the Supplementary Material. The symmetry parameter distinguishes between solid and liquid phases, so melting and recrystallization dynamics can be traced.

target breaks at about 300 ps. The ablated liquid layer disintegrates into two large droplets of about 25 − 30 nm size.

The pressure evolution in the target during the first 13 ps after the absorption of 90 mJ/cm^2 is shown in Fig. 6. The amplitude of the frontal tensile wave TW_F decreases with increasing temperature and, hence, is lower compared to the case of 60 mJ/cm^2. The tensile strength of the material also decreases with temperature. So, although the tensile pressure is weaker, it is sufficiently strong to create a cavitation zone in the near surface region below the ablated top layer. This cavitation zone is labeled C_1 on the density map at t = 15 ps, shown in the inset in Fig. 6.

As discussed above, the compressive wave partially reflects from the mechanically softer substrate (the acoustic impedance of Si is smaller than that of Ru) and, as a result, the reflected tensile wave TW_R propagates from the interface back to the surface. The superposition of the two tensile waves, $TW_F + TW_R$ creates a second cavitation zone C_2 deeper than the first one. Both cavitation zones are clearly observed on the density profile at t = 15 ps, shown in Fig. 6 with a dashed line. Further material evolution results in stretching of the first cavitation zone and collapse of the second one. The density map at t = 50 ps in Fig. 5 (a) shows the stretched cavitation zone C_1 and the remainders of the cavitation zone C_2 in the form of a few small cavities.

A similar pressure evolution (not shown) and, hence, similar ablation process occurs in the case of 120 mJ/cm^2 of absorbed fluence, see the mass distributions in Fig. 5 (b). A minor difference between the 90 mJ/cm^2 and the 120 mJ/cm^2 is that in the latter case the cavitation zone gradually grows into the depth of the sample following the propagation of the frontal tensile wave. No distinct two layers of cavitation

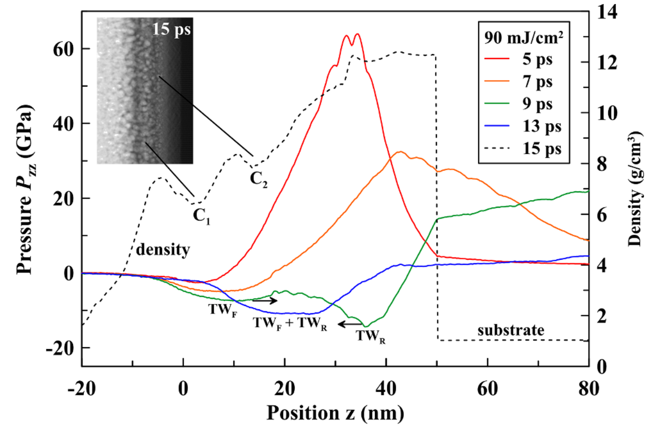

Fig. 6. Evolution of pressure in the Ru-on-substrate target irradiated with a 100 fs XUV laser pulse. The absorbed fluence is $F_{abs} = 90$ mJ/cm^2. The density profile at $t = 15$ ps is shown with the dashed line on the same graph. The density map at $t = 15$ ps is shown in the inset. The two cavitation zones, C_1 and C_2, are clearly visible and are formed with the frontal tensile wave TW_F and with the superposition of the frontal and the reflected waves $TW_F + TW_R$, respectively.

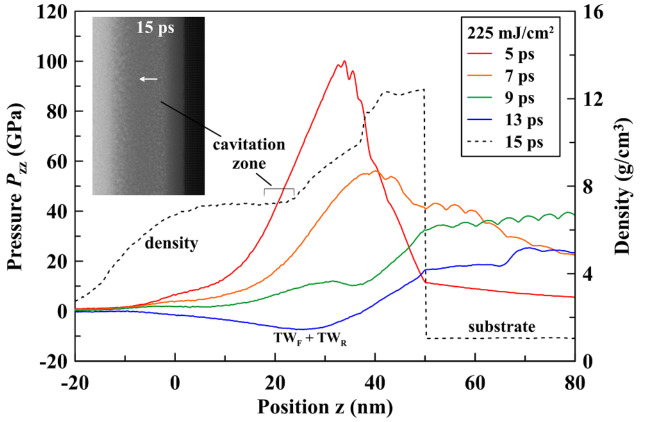

Fig. 7. Evolution of pressure in the Ru-on-substrate target irradiated by a 100 fs XUV laser pulse. The absorbed fluence is $F_{abs} = 225$ mJ/cm^2. The density profile at $t = 15$ ps is shown with the dashed line on the same graph. The density map at $t = 15$ ps is shown in the inset. The cavitation zone is formed with the superposition of the frontal and the reflected waves $TW_F + TW_R$. The white arrow shows the direction of the expansion of the cavitation zone with time.

are observed. Another difference between these two cases is that the ablating layer does not disintegrates into droplets in the case of 120 mJ/cm^2, but stays intact. That may be an effect of periodic boundary conditions that can stabilize the ablating layer. We investigate the behaviour of the ablating layer in Section 3.4.

A different situation is realized at the highest considered absorbed fluence of 225 mJ/cm^2, Fig. 5 (c). Due to the extremely high atomic temperature of $20 - 30$ kK reached in the thin subsurface region of Ru during the first few ps after absorption, the pressure remains strictly positive until the frontal compressive wave is reflected from the Ru-substrate interface, see the pressure profiles in Fig. 7. The superposition of the waves $TW_F + TW_R$ creates sufficiently strong tensile pressure and the cavitation zone is formed at a depth of about 20 nm. This cavitation zone is clearly observed on the density map shown in the inset of Fig. 7. The cavitation zone grows in the direction shown with a white arrow.

As one can see from Fig. 5, Ru under femtosecond XUV exposure exhibits two-level ablation in a wide range of fluences near and well above the ablation threshold. The top few nm layer ablation is followed by ablation of a thicker layer. As shown above, the latter occurs due to the tensile wave, either purely by the frontal one or by the superposition of the frontal and the reflected one.

The mechanism responsible for the thin top layer ablation depends on the fluence. For low fluences $60 - 90$ mJ/cm^2 the frontal tensile wave results in cavitation and ablation of the top material. Even low stresses produced by the tensile wave are sufficient for rupture, since the significantly heated liquid has a low tensile strength. For higher fluences, the pressure is strictly positive during the first few ps, whereas the ejection of material has already begun. This means that ablation of the top thin layer occurs not via thermo-mechanical cavitation, but due to the expansion of the liquid which phase state runs from an initial high-temperature state towards the subcritical or supercritical thermodynamic state. Expansion to a subcritical condition may result in the formation of gas–liquid mixture ejecta via overheating and fast explosive boiling of the hot liquid [72]. The supercritical ablation consists in a continuous formation of hot gas ejecta without phase separation into vapour and liquid [73].

To illustrate different mechanisms of top layer ablation we show the atomistic configuration of the top Ru part at $t = 20$ ps in case of $F_{abs} = 120$ mJ/cm^2, see Fig. 8. Three characteristic regions can be identified: hot gas of Ru atoms in the top part (supercritical ablation), hot gas–liquid mixture (subcritical ablation), and cavitation zone created by the tensile wave. The corresponding temperature and density profiles are also shown. It is worth to note that the negative pressure is generated only in the cavitation zone and causes the deceleration of material there.

The critical parameters of Ru modeled with the EAM interatomic potential are extracted from separate MD-MC calculations using the phase coexistence method. The results are $T_c = 14500$ K, $P_c = 0.19$ GPa and $\rho_c = 1.1$ g/cm^3. The atomic temperature of the Ru top surface rises

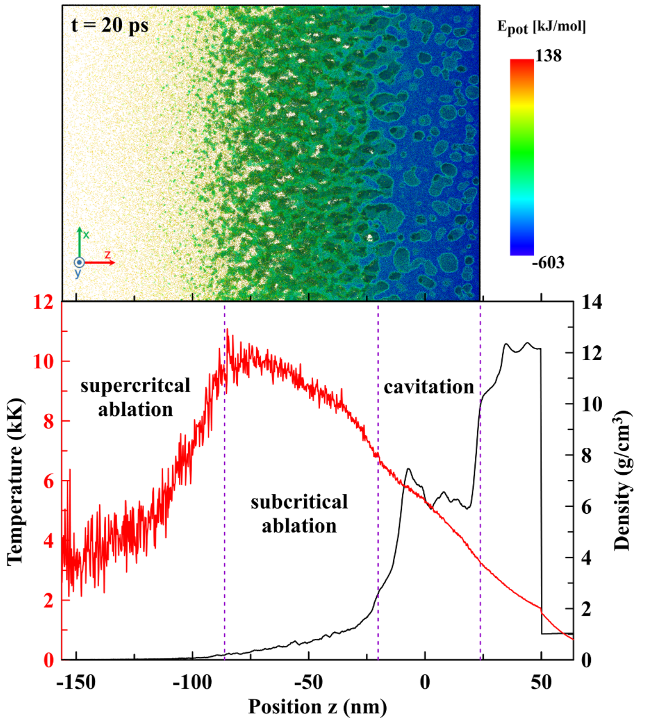

Fig. 8. Top panel: phase structure of material flow at $t = 20$ ps induced by $F_{abs} = 120$ mJ/cm^2. The atoms are coloured according to their potential energy. The leading expanding gas on the left is produced in supercritical expansion of a top hot layer with a thickness of $1 - 2$ nm. It follows by a two-phase gas–liquid zone formed via fragmentation of a hot liquid expanding along a subcritical adiabat. This zone is followed by a dense foam-like material formed via cavitation of relatively cold liquid stretched by the negative pressure. Only the last zone is subjected to deceleration and a Rayleigh-Taylor instability may develop here, see Section 3.4. Bottom panel: the corresponding temperature and density profiles.

above 16 kK during the first few ps after the absorption of 120 mJ/cm^2, while the density drops below 2 g/cm^3, which confirms that both subcritical and supercritical ablation mechanisms are possible. A similar situation is realized for higher fluences.

3.4. *Dynamics of ablating layer*

Fig. 5 suggests that the thick ablating layer exhibits inconsistent behaviour with increasing fluence. With our MD-MC simulations we found that the layer stays stable at fluences of 120 and 150 mJ/cm^2, whereas for other considered fluences (lower as well as higher) it disintegrates into liquid droplets. In this section we investigate possible reasons of unstable evolution of the ablating layer.

3.4.1. *Rayleigh-Taylor instability*

It is known that development of Rayleigh-Taylor instability (RTI) can induce fragmentation of ablating material [74]. Such a phenomenon may occur when a more dense liquid (Ru in our case) is expanding into a less dense environment (vacuum or vapour in our case) and is being affected by a strong deceleration. The deceleration of the target surface is produced by a subsurface pressure gradient directed towards the vacuum, which generates a corresponding force directed to the bulk of the target. Just after absorption of a laser pulse, the pressure under the surface has a large positive value which produces the pressure gradient directed to the target, and thus this gradient causes expansion of the material and acceleration of the surface. Then, the subsurface pressure decreases, and if it drops below the vapour pressure above the surface, the pressure gradient changes its sign and begins decelerating the target surface. The sign change of the subsurface pressure gradient is clearly visible in Fig. 7, where it happens after 9 ps.

Such a decelerating pressure gradient results from two sources. First, it is a result of stretching of a continuous subsurface material at an early stage of the expansion. Then, after cavitation of the stretched liquid, it also results from the tension of the foam-like material in the cavitation zone that may pull the ablating layer back to the target during a long time until the foam ruptures. It is clear that the cohesive forces of continuous liquid are much stronger than the capillary forces in the foam, which results in a huge deceleration at the early stage of expansion and a relatively small deceleration after cavitation.

To investigate whether the RTI plays a role in Ru ablation, we analyze the velocity of the ablating layer in the case of $F_{\mathrm{abs}} = 120$ mJ/cm^2. At each time step we record the velocity of the top material at a density level of 6 g/cm^3, which is an average density in the ablating layer. Knowing the velocity, we calculate the deceleration of the layer. The results are shown in Fig. 9. Please note that z axis is directed in the depth of Ru, hence the negative sign of velocity directed to the vacuum. An enormously strong deceleration of the top material is observed during the first 15 − 20 ps. Further stretching of the cavitation zone weakens the force that pulls the ablating layer back, since the net cross-section surface line of cavities in the binding foam-like material decreases due to the reduction of the number of cavities and increase of their sizes.

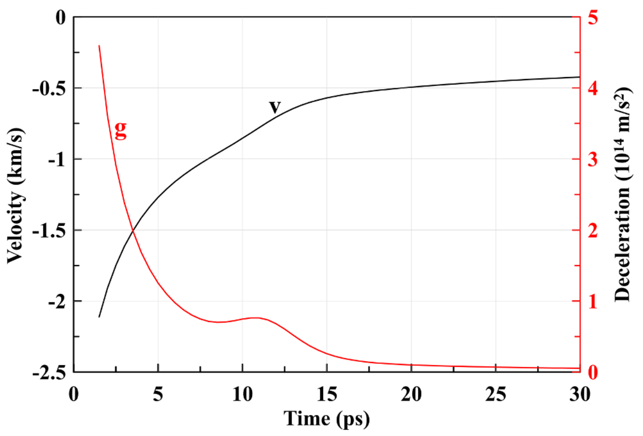

Fig. 9. The time dependence of the velocity and deceleration of the ablating liquid layer calculated for the case of $F_{\mathrm{abs}} = 120$ mJ/cm^2, see Fig. 5 (b).

To check if such a large deceleration acting on the ablating layer over a short timescale is sufficient to cause the RTI development, we calculate the characteristic RTI growth rate γ:

$$\gamma(t) = \sqrt{\mathrm{At}g(t)k - k^3\sigma/\rho}. \tag{1}$$

Here $g(t)$ is deceleration, $k = 2\pi/\lambda$ is the wave number of the surface profile perturbation with wavelength λ that may develop due to the deceleration, At is an Atwood number, which is equal to 1 in the case of vacuum, σ is the surface tension, and ρ is the density of the liquid Ru layer. The expression (1) is taken from [75] with the viscosity of liquid Ru ν not taken into account ($\nu = 0$). Here we only aim to get an estimation of γ and obtain a qualitative criterion for the RTI development. The average density of the ablating layer is 6 g/cm^3. For the surface tension we take $\sigma = 1.6$ J/m^2 at $T = 5000$ K, see Appendix B. The latter is the average temperature of the ablated layer at the considered timescale.

As a criterion of the RTI strength we use exponential amplification in the linear perturbation amplitude in the quasi-classical approximation [74]:

$$a(t)/a(t_0) = \exp\left(\int_{t_1}^{t} \gamma(t')dt'\right). \tag{2}$$

Here $a(t_0)$ is a small nanometer-scaled amplitude of the initial perturbations, and integration starts from the onset time t_1 when the boundary between the subcritical and cavitation zone is formed, see Fig. 8. In our case it is around 5 ps. Only starting from this time the RTI can develop. The amplification is calculated for different perturbation wavelengths λ and is shown in Fig. 10. The maximum allowed wavelength is equal to the largest MD box dimension, 128 nm in our case. The amplification stops to increase at the moment when the surface tension σ dampens the perturbation for the considered λ (root expression in (1) becomes zero). One can see that for all considered λ the amplification of the initial perturbations with nano-scaled amplitudes is below a factor of 4, which is not sufficiently large to cause fragmentation of the ablating layer.

The perturbation $\lambda = 10$ nm is considered with the aim to explain the development of liquid jets at the border of the ablating surface at the early stage of ablation, see, for example, Fig. 5 (a) at $t = 50$ ps. Such stretched liquid jets is not a typical feature of explosive boiling. The lateral size of these jets is around 10 nm. As one can see from Fig. 10, such a perturbation is short-lived and is damped by the surface tension

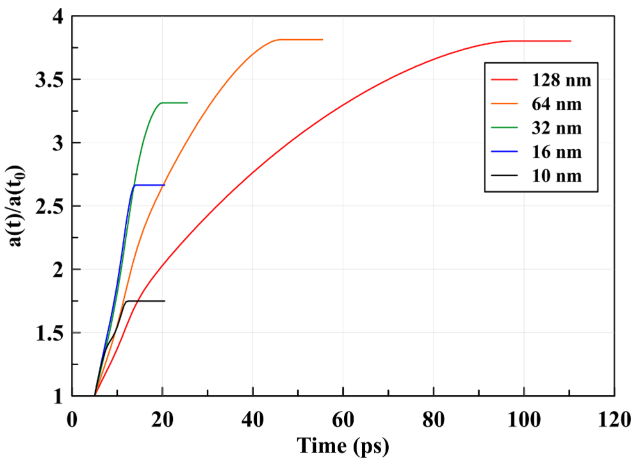

Fig. 10. RTI amplifications of small perturbations with different wavelengths. Amplifications are saturated after the deceleration drops below $g = k^2\sigma/\rho/\mathrm{At}$.

after 12 ps. The value of surface tension is taken to be $\sigma = 1.03\ \mathrm{J/m^2}$, which corresponds to $T = 7000$ K. The resulting amplification is below a factor of 2, which is insignificant.

The stretching of the liquid jets at the border of the ablating surface can be explained by the difference in the velocity between the ablating surface, which is strongly decelerated, and the velocity of the jet attached to it.

In the study of gold ablation into water, for example, amplification of 50 and higher was required for the RTI to play a noticeable role, see Fig. 31 at $t = 297.6$ ps and corresponding amplification in Fig. 30 in the Ref. [74]. Such a large amplification is achieved because of a long action of deceleration onto the gold-water boundary. In contrast, stronger deceleration of Ru ablating into vacuum, considered in this work, acts over a very short time, not sufficient for the RTI to develop. When gold ablates into vacuum, which is also considered in Ref. [74], the RTI does not develop due to a large thickness (large inertia) of the ablating layer and a low surface tension of gold (low tensile strength of binding foam). But in the case of Ru, even with the factors favourable for the RTI development, namely small thickness of the ablating layer and high surface tension, the effect of the RTI is insignificant. Other possible reasons of layer disintegration will be discussed in the next section.

3.4.2. Nonuniform fluence profile

As was already mentioned, the periodic boundary conditions applied in lateral directions can affect the evolution of the ablating layer by stabilizing it. To reduce a possible size effect, we performed a calculation with an increased MD box size. We increase L_x to 512 nm, so the resulting MD box has a size of $512 \times 32 \times 150\ \mathrm{nm^3}$ and contains ~183 million atoms.

Moreover, instead of a top-hat fluence profile we use

$$F(x) = F_e + (F_p - F_e)\cos^2(\pi x/L_x). \tag{3}$$

Such a profile provides a peak fluence F_p in the center of the MD box and F_e fluence at the edges. A $\cos^2(\pi x/L_x)$ function is chosen due to its periodicity, which is dictated by the periodic boundary conditions, and due to its similarity to a Gaussian function, which realistically represents a spatial energy distribution in a laser pulse. With this simulation we aim to investigate how a nonuniform fluence distribution would affect the dynamics of the ablating layer.

Such a more realistic representation of a laser pulse in our simulations comes at the expense of losing accuracy in modeling non-reflecting boundary condition and in mimicking heat conduction in a thick substrate. Due to a nonuniform fluence distribution, the history of a LP will be different for different x coordinates. For simplicity, we use the history of a Lagrangian particle (LP) at the averaged fluence for the entire length of the simulation box. Since with this simulation we are interested in the short-term dynamics of the ablating layer and not in the recrystallization process, our simplified one-dimensional LP formalism should be sufficiently accurate to provide a reliable qualitative picture of the ablation dynamics. The LP formalism is described above in Section 2.3. The main novelty of our model is the ability to simulate interaction of high energy photons with matter, preserving a large spatiotemporal scale of the simulations. The applicability of the Monte Carlo and hydrodynamics parts of the model to the cases of much higher photon energy was demonstrated in the previous work [53].

The disintegration of the ablated layer can be a result of the interplay between various factors, such as surface tension and its temperature dependence, parameters of the cavitation zone, and thickness of the ablating layer. The mass distribution at 150 ps shown in Fig. 11 illustrates that the ablating layer is pulled back nonuniformly by the remaining material in the cavitation zone, which is a possible source of instability. Another possible explanation of the fragmentation into droplets is the existence of cavities in the ablating layer.

With the simulations presented in Fig. 11 it is possible to get insights into another important process – formation of the crater edge. The evolution of the ablating layer can be described with the following stages: (i) formation of the layer, (ii) expanding of the layer into vacuum, (iii) fragmentation that starts in the center and propagates towards the edge, and (iv) recrystallization of the remaining part at the edge. The interplay between the last two processes defines the final structure of the crater edge, see the inset in Fig. 11 at $t = 450$ ps. Although, as mentioned above, the process of recrystallization is not modeled quantitatively accurate, this calculation provides us with a qualitative description of the key processes leading to crater edge formation.

In the following section we compare the results of our simulations with the available experimental data obtained in single-shot damage threshold experiments.

4. Fluence thresholds and damaged surface morphology

The single-shot damage experiments were performed at the free electron laser in Hamburg (FLASH), where Ru polycrystalline films of 50 nm thickness on a single-crystal Si substrate were exposed to 100 fs FWHM, XUV (92 eV or 13.5 nm) laser pulses with various fluence. The detailed description of this experiment together with the *post-mortem* analysis of damage craters is reported in [57]. The goal of this section is a detailed explanation of the existing experimental data using our simulations. First, we briefly recall the main experimental results.

The development of the damage morphology with increasing fluence can be studied within a single damage spot. A high-resolution scanning electron microscopy (HR-SEM) image of a typical crater produced in Ru is shown in Fig. 12 (a). Visible damage starts with increased surface roughness near the edge of the crater (area 1). Inside the crater, where ablation of material occurs, there are two characteristic zones: a rough periphery (area 2) and a flat central part (area 3), separated by a distinct crack. The roughness in area 2 gradually decreases towards the center of the crater, which is illustrated with an AFM line profile, Fig. 12 (b), taken through the center of the damage spot as indicated with a dashed line in Fig. 12 (a).

The peak incident fluence of the laser pulse that produced this crater was measured to be $374 \pm 75\ \mathrm{mJ/cm^2}$, which corresponds to $109 \pm 22\ \mathrm{mJ/cm^2}$ of absorbed fluence, if one takes into account the surface reflectivity (68%) and a calculated fraction of energy that escapes from the surface via photo- and secondary electrons (~9%) [57]. For convenience we continue our analysis only in terms of the absorbed fluence. The ablation threshold was determined by Liu's plot method [76] to be $F_{\mathrm{abl}}^{\mathrm{exp}} = 58 \pm 12\ \mathrm{mJ/cm^2}$. The flattening phenomenon in the center also exhibits a threshold behaviour with a threshold fluence $F_{\mathrm{flat}}^{\mathrm{exp}} = 91 \pm 18\ \mathrm{mJ/cm^2}$. The crater depth in the flat area is constant and is equal to 23 nm, see Fig. 12 (b).

A HR-SEM image of a damage spot produced with a peak fluence $92 \pm 18\ \mathrm{mJ/cm^2}$, which is just at the flattening threshold, is shown in Fig. 13. As one can see, no distinct flat area in the center of the crater has developed yet.

In order to reveal the in-depth structure of a damage crater a transmission electron microscopy (TEM) cross section is taken in the area indicated with a dashed yellow line in Fig. 13. The TEM image is shown in Fig. 14. One can see the undamaged part of the Ru film, the edge of the crater, and the morphology inside the crater. The edge of the crater is formed during the process of recrystallization of the remaining part of the ablating layer, see Fig. 11. The roughness of the surface inside the crater decreases towards the center, where the local fluence is higher, which is consistent with the AFM cross section in Fig. 12 (b).

The results of the MD-MC simulations are shown in Fig. 14 together with the TEM image in the same scale for a one-to-one comparison. Note, that the simulations with the top-hat fluence profile and various fluence levels are considered in this section, same as in Section 3.3. In such a way we probe different positions along the damage crater, corresponding to a different locally absorbed fluence. Computation of the

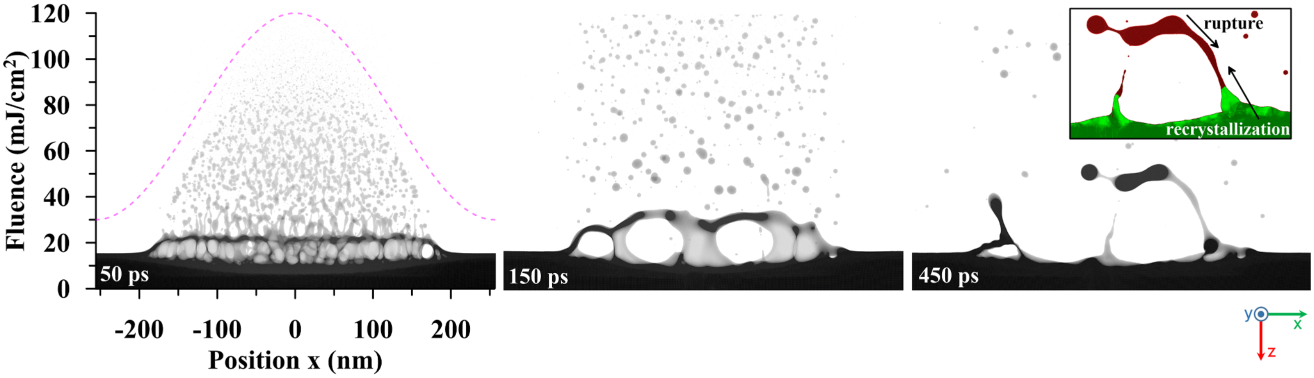

Fig. 11. Maps with mass distributions illustrating the ablation of Ru obtained with a large-scale MD-MC simulation. The fluence profile of an XUV 100 fs laser pulse is taken according to expression (3) and is shown with a dashed line. The inset shows a symmetry parameter distribution with green colour corresponding to a solid phase and red colour to a liquid phase. The bottom arrow shows the direction of the recrystallization front propagation. The top arrow illustrates that the rupture of the liquid ablating layer propagates from the center towards the edge. The dynamics of these processes defines the final structure of the crater edge.

whole damage spot of several μm size is, of course, not possible to accomplish in reasonable time with the available computer power.

The end results of the simulations are shown in Fig. 14, namely completely recrystallized targets after the irradiation procedure. Only the Ru part of the sample is shown with the MD-MC mass distributions, the substrate is schematically shown with a grey rectangle. No visible damage to the substrate was detected in all performed simulations. The arrows approximately indicate the correspondence between the simulation results and the experimentally determined morphology. The result with the highest considered fluence of 225 mJ/cm^2 is shown for a complete picture of the surface morphology evolution with increasing fluence, but significantly exceeds the experimental fluence.

The pre-ablation regime with cavitation, F_{abs} = 45 mJ/cm^2, see Fig. 3 (a), results in the formation of the surface with increased roughness after the complete resolidification. The roughness and insignificant swelling of the surface are caused by the small subsurface cavities that got frozen by the resolidification front. That explains the surface morphology outside the damage crater (area 1 in Figs. 12 and 13). The existence of the frozen subsurface cavities after the irradiation of the targets with a laser was also reported for other metals [77–79].

In the case of F_{abs} = 60 mJ/cm^2 no significant ablation occurs, only a thin top layer is removed, see Fig. 3 (b). That case can be considered as just slightly below the experimentally detected ablation threshold. We suppose that ablation of a thin few nm layer via sub- and supercritical mechanisms discussed above is another contribution to the formation of a rough surface outside the experimental crater.

The onset of the ablation of a thicker layer is detected for a fluence F_{abs} = 75 mJ/cm^2. The final frozen Ru surface for that case is shown in Fig. 14. While a part of the material was ablated, the other part did not overcome the surface tension, got pulled back to the surface and remained frozen in the form of a large droplet with a size of about 30 nm. Therefore, with our MD-MC simulations we define the ablation threshold to be around $F_{\text{abl}}^{\text{MD-MC}} = 60 - 75$ mJ/cm^2, which is in a very good agreement with the experiment.

A series of simulations with a fluence $F_{\text{abs}} = 90 - 150$ mJ/cm^2 demonstrates the decrease of the frozen surface roughness with increasing fluence. The average crater depth, extracted from the calculation of the amount of removed material, increases from 11 nm for F_{abs} = 90 mJ/cm^2

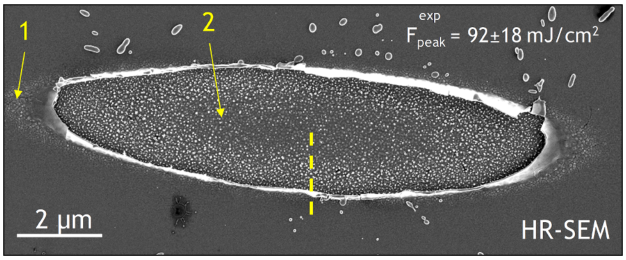

Fig. 13. HR-SEM image of a single-shot damage spot produced in Ru with a 100 fs XUV FEL pulse. The peak absorbed fluence is $F_p = 92 \pm 18$ mJ/cm^2. The labels 1 and 2 indicate the characteristic damage morphologies: increased roughness outside the crater and rough surface inside the crater, respectively. No distinct flat area in the center is detected. A dashed line indicates where the TEM analysis is performed, see Fig. 14.

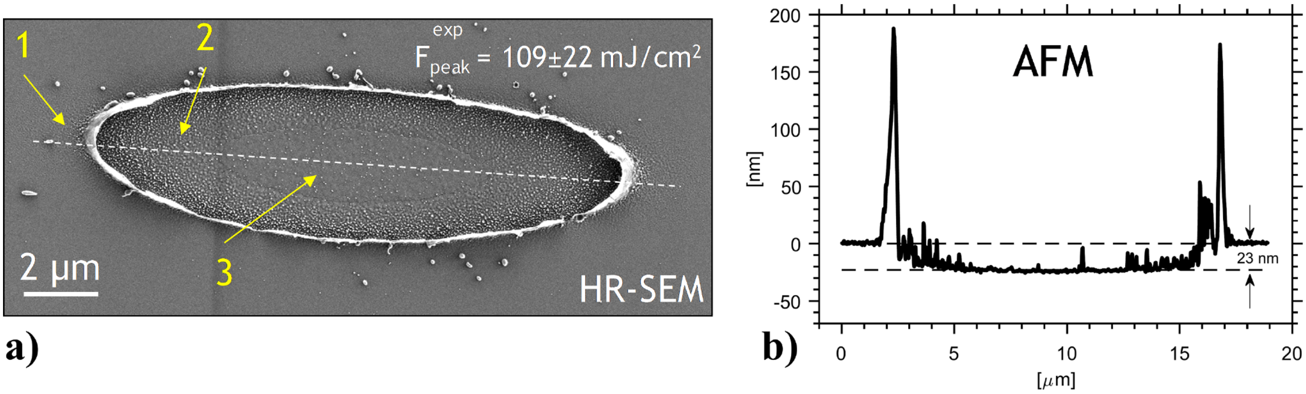

Fig. 12. (a) HR-SEM image of a single-shot damage spot produced in Ru with a 100 fs XUV FEL pulse. The peak absorbed fluence is $F_p = 109 \pm 22$ mJ/cm^2. The labels 1,2 and 3 indicate the characteristic damage morphologies: increased roughness outside the crater, rough periphery and flat center inside the crater, respectively. The dashed line indicates where the AFM line profile was measured. (b) AFM line profile illustrating the decrease of the surface roughness at the bottom of the crater from the edge towards the center.

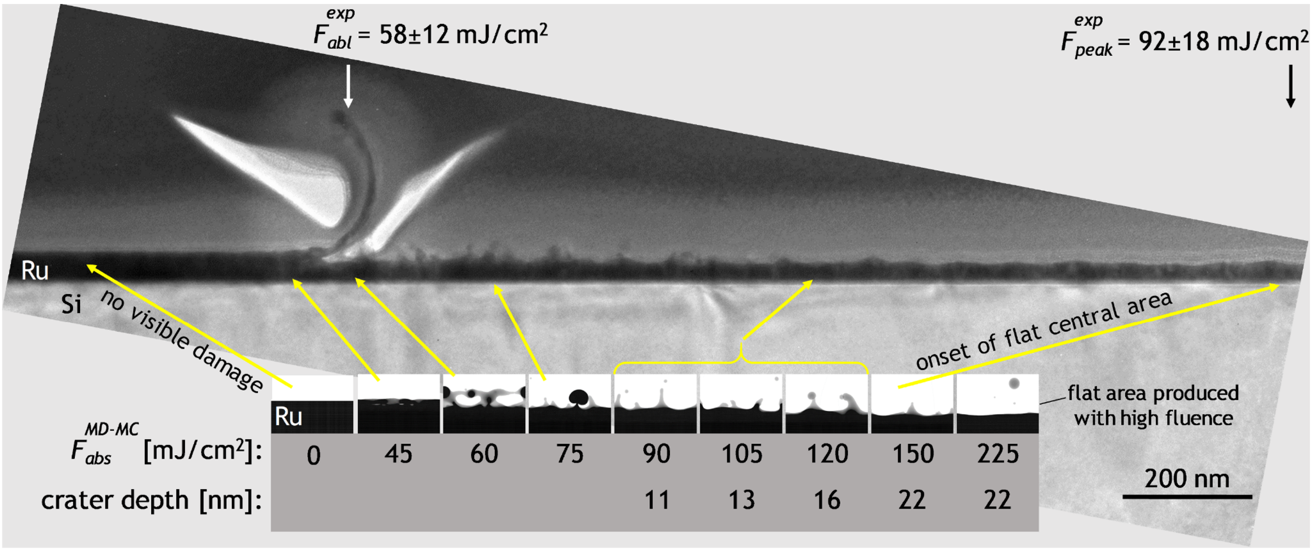

Fig. 14. Comparison of the MD-MC simulations with the experimental damage morphology obtained with a TEM cross-section. TEM image shows the vicinity of the crater edge and the morphology inside the crater. The MD-MC results are shown below and represent the mass distributions of Ru at the end of the simulations, i.e. when Ru is totally recrystallized. The substrate is shown schematically with a grey rectangle. The scale of the TEM image and the MD-MC results is the same, enabling one-to-one comparison.

to 22 nm for F_{abs} = 150 mJ/cm^2, which is also in a very good agreement with the experiment. The case of F_{abs} = 150 mJ/cm^2 can be considered as the onset of the flat central area (area 3 in Fig. 12), which serves as our model estimation of the flattening threshold.

As one can see, our model overestimates the flattening threshold, but provides an accurate description of the surface morphology trend with increasing fluence. The deviation from the experiment in the limit of high fluence may result from the lack of reliable knowledge of the Ru parameters at sub- and supercritical conditions. Calculations made with the EAM potential of Ru developed in this work (see Appendix B) may overestimate the critical parameters of Ru, which, unfortunately, are not known.

The highest considered fluence of F_{abs} = 225 mJ/cm^2 demonstrates the flat frozen surface. The crater depth of 22 nm agrees well with the experimental value of 23 nm in the central part of the crater, see Fig. 12 (b).

The morphology of the bottom of the crater is determined by a local absorbed fluence. Two key processes play a crucial role here: the hydrodynamic evolution of the top molten material and the rate of the heat dissipation from the top hot region to the deeper cold part of the material. For relatively low fluences, the characteristic time of hydrodynamic motion of ablating material is longer than the characteristic time of its resolidification, which leads to the formation of the rough bottom of the crater. For higher fluences, the characteristic time of material ablation and smoothing of the remaining molten material by surface tension is shorter than the characteristic resolidification time, which leads to the formation of the flat frozen surface in the central part of the crater. Dynamics of melting, ablation and recrystallization for fluences F_{abs} = 90, 120 and 225 mJ/cm^2 is illustrated with the movies, that can be found in the Supplementary Material.

5. Discussion

We reported simulation results on the dynamics of the Ru damage in pre- and above ablation regimes induced by femtosecond XUV laser pulses. The simulations were performed with our new hybrid computational scheme that overcomes several limits of the previous models and is applicable in a wide range of laser parameters and materials:

- **Photon energy** from XUV to hard X-rays. Relativistic effects restrict the photon energy to ~10^5 eV. To consider optical photon energy and below, the initial MC part of our model must be replaced with a Boltzmann kinetic equation, or a TTM-based approach if applicable.
- **Fluence** is restricted to a maximum value in the following way. First, the fluence must not be too high, otherwise the density of the excited electrons will become comparable to or higher than the atomic density of the target, and XCASCADE(3D) will not be applicable. Second, in the HD and MD parts of the model, the equation of state and interatomic potential, respectively, should properly reproduce the material properties at sub- and supercritical conditions when the fluence becomes considerably high, otherwise unrealistic results can be obtained. Third, the fluence should stay below the threshold for plasma formation. In this work, the highest fluence F_{abs} = 225 mJ/cm^2 can be considered at the limit of the model applicability, since it already brings Ru to a supercritical state. Further increase of the fluence requires dedicated studies.
- **Pulse duration** should be sufficiently short, so one can assume that absorption of all the photons in a laser pulse occurs in the unmodified target. The particular applicable values of the pulse duration depend on the fluence. The higher the fluence, the sooner the material is modified, the shorter the pulse duration should be. For metals in the fluence regime near the ablation it is typically restricted to ~1 ps.
- **Any metal** can be considered, as long as its 2T equation of state, 2T thermal conductivity, electron–phonon coupling factor and interatomic potential are known in a wide range of density, temperature and pressure. In the context of ablation, the following properties are important to reproduce with the MD interatomic potential: melting temperature, stress–strain curve, surface tension and its dependence on temperature (see Appendix B).

The main novelty of our model is the ability to simulate interaction of high energy photons with matter, preserving a large spatiotemporal scale of the simulations. The applicability of the Monte Carlo and hydrodynamics parts of the model to the cases of much higher photon energy was demonstrated in the previous work [53].

The disadvantage of our approach is a lack of completely reliable description of lattice evolution on an atomistic level during the first 3 ps (as described in Sections 2.2 and 3.2). However, there are no significant 3D spatial and phase modifications in the material during that time, so the applicability of the 2T-HD model to describe that stage of material evolution is justified. Improving this part of the model may be considered as a next step in our hybrid model development. As an alternative, the TTM-MD method (with the electronic pressure included [37]) could be used, provided with the heat source from the XCASCADE (3D). This method, although different in technical details, takes into account the same physical processes, so similar results are expected.

Taking into account possible nonequilibrium behaviour of the ionic system would require a different, significantly more complex approach (such as e.g. Boltzmann kinetic equations) instead of two-temperature-based formalisms, which would have a larger computational cost. It is beyond the scope of the present work, since here we are mostly interested in the process of ablation and formation of the final frozen surface structures.

The model was applied to the XUV irradiated Ru with the focus on an atomistic picture of damage development, since such details of femtosecond ablation dynamics of Ru were never studied before. The parametrization of Ru in the 2T state [64] used in this work was obtained via ab initio calculations and, to the best of our knowledge, is the most accurate theoretical data on Ru in the studied context. The electron-phonon coupling factor exhibits a decrease with an increasing electron temperature [64], similar to some other transition metals such as iron, nickel and platinum [80]. The decrease is not significant compared to a constant coupling factor (taken at $T_e = 0$, for example), and can only slightly influence the quantitative characteristics of the ablation process. A reliable interatomic potential for Ru applicable for various high-energy high-pressure studies was developed for the first time (see Appendix B) and can be found in the Supplementary Material.

General mechanisms of femtosecond ablation that are common for various metals were found to be responsible for XUV induced damage in Ru, although with several non typical effects. We found that ablation threshold is twice higher than the cavitation threshold, which is not typical compared to the previously studied optically excited metals such as Au [36] and Al [81]. For these metals with a large heat affected zone and a thick ablation layer the cavitation and ablation thresholds are close to each other. We interpret the large difference between the two thresholds in our case as a result of a large surface tension of Ru and a small heat affected zone (thin ablation layer).

According to our simulations, a two-level ablation occurs in Ru in a wide range of fluences near and well above the ablation threshold. For lower fluences in that range both levels are ablated due to a tensile component of the generated pressure wave, whereas for higher fluences the top thin layer is ablated via sub- and supercritical decomposition into a gas–liquid mixture. Other studied metals typically exhibit ablation of a relatively thick single layer via a thermo-mechanical mechanism (tensile wave) [36,59], whereas complex ablation of the top material involving sub- and supercritical decomposition, also referred to as phase explosion, with simultaneous cavitation in the deeper parts is found only at fluences significantly higher than the ablation threshold [81,82].

The two-level ablation in Ru even at relatively low fluence near the ablation threshold occurs due to the high density of the absorbed energy in the surface layer during the initial stage of the Ru evolution. Such confinement of energy transferred to the ionic subsystem of the surface layer is realized due to (i) the irradiation conditions, namely absorption of XUV light at 20° grazing incidence, which occurs in the top 3.5 nm layer, (ii) the XUV induced electron cascades spreading the energy only insignificantly, and (iii) the Ru thermal properties, namely a relatively low electron thermal conductivity and a strong electron–phonon coupling factor, which provides the transfer of energy from electrons to the ions faster than the stress relaxation via expansion of heated material. Altogether it creates a small heat affected zone with a high temperature and pressure even at relatively low fluence near the ablation threshold. One would need a considerably higher fluence to reach a similar two-level ablation in materials where the heat affected zone is large, such as Au or Al.

We showed that disintegration of the ablating layer is unlikely to be caused by the development of a Rayleigh-Taylor instability, but is rather a result of a large surface tension of Ru, see Fig. 11. To get more insight into this process, the dynamics of the ablation process can be investigated with pump–probe experiments. It is known that one can observe the transient Newton's rings (NRs) during the ablation process by using the time-resolved microscopy technique [83]. The NRs result from the interference of light reflected from the ablating layer and the remaining part of the target [84]. The existence of the NRs on a long nanosecond timescale, known for example for such metals as Al, Au, Ti, Ni [83,85], means that the ablating layer stays stable during that time. On the other hand, the short lifetime of the NRs observed using a soft X-ray probe was reported for W and Pt, and was attributed to the rapid growth of the surface roughness of the ablating layer [86]. MD simulations of Pt ablation showed disintegration of the ablating layer into droplets [87], confirming the experimental findings. We suppose that high surface tension in combination with small thickness of the liquid ablating layer are necessary conditions for layer disintegration.

Dedicated experimental studies are required to complement the simulation results presented in this work in order to get more insight into the transient evolution of the ablating layer. Such pump–probe experiments are outside the scope of the present paper.

The rigorousness of our simulations is illustrated with a quantitative agreement with the previously reported experimental results [57] on ablation threshold fluence, crater depth and fine details of the crater damage morphology. For the first time, frozen (i.e. final) structures at the bottom of the crater and their dependence on the absorbed fluence level were described. It was shown that heat removal plays a key role in the formation of these structures. Namely, in the case when heat removal is hindered and Ru is in a melted state for a relatively long time, there are no frozen structures at the bottom of the crater – the bottom is smooth.

Our simulation with a nonuniform fluence profile explains the mechanism of the crater edge formation. The edge which appears as a rim around ablation craters is observed practically in all laser ablation experiments (see, for example, Fig. 12 (b) and Refs. [5,77,78]). Previous explanation of the edge formation as a result of frozen subsurface cavities is complemented with our analysis presented in Fig. 11. We show that the edge can be formed during the recrystallization of the remaining part of the ablated layer, after a detachment of a central part of the layer. The mechanism of the crater edge formation defines its position, which is important for quantitative measurements of the ablation threshold by Liu's plot method [76].

The results obtained in this work are of course sensitive to a particular choice of the thermo-mechanical parametrization of Ru in the two- and one-temperature stage. The parameters used in the 2T-HD calculations (the most important ones are temperature dependent heat capacity, electron thermal conductivity and electron–phonon coupling, see Ref. [64]) and the interatomic potential (see Appendix B) were obtained from first-principal calculations, and, to the best of our knowledge, are the most accurate data on Ru in the context of femtosecond laser ablation. A good agreement of our simulations with the ablation experiment validates the parametrization used.

6. Conclusions

A new hybrid computational approach that combines Monte Carlo, hydrodynamic and molecular dynamic models was developed and applied to study the dynamics of femtosecond XUV laser damage in Ru thin films. The model is based on previously reported solutions and extends its applicability to a wide range of irradiation conditions covering the full timescale of material evolution.

The studied irradiation parameters were chosen in accordance with the previously reported single-shot damage experiments. Due to the grazing incidence of the XUV laser pulses (small photon penetration depth), insignificant XUV-induced electron cascading and Ru thermal properties (low thermal conductivity and large electron–phonon coupling factor) the heat affected zone is small, resulting in a high energy density in the surface region even for relatively low fluences. Such a distribution of the absorbed energy results in a two-level ablation in a wide range of fluence near and well above the ablation threshold.

Large scale atomistic simulations were carried out until a complete resolidification of Ru is reached, which opens up a possibility of a direct one-to-one comparison with the experimental results on damage crater morphology. We achieved a quantitative agreement between the simulations and the experiment in ablation threshold fluence, crater depth and frozen structures on the bottom of the crater, and explained the responsible damage mechanisms.

CRediT authorship contribution statement

I. Milov: Conceptualization, Software, Validation, Investigation, Data curation, Writing - original draft, Visualization. **V. Zhakhovsky:** Conceptualization, Methodology, Software, Validation, Data curation, Writing - review & editing, Supervision. **D. Ilnitsky:** Methodology, Software, Validation, Data curation. **K. Migdal:** Methodology, Software. **V. Khokhlov:** Methodology, Software. **Yu. Petrov:** Methodology, Software. **N. Inogamov:** Methodology, Software, Writing - review & editing. **V. Lipp:** Methodology, Software, Validation, Data curation, Writing - review & editing. **N. Medvedev:** Methodology, Software, Writing - review & editing. **B. Ziaja:** Methodology, Writing - review & editing, Supervision. **V. Medvedev:** Project administration. **I.A. Makhotkin:** Supervision, Project administration. **E. Louis:** Writing - review & editing, Supervision, Project administration, Funding acquisition. **F. Bijkerk:** Writing - review & editing, Funding acquisition.

Declaration of Competing Interest

The authors declare that they have no known competing financial interests or personal relationships that could have appeared to influence the work reported in this paper.

Acknowledgements

Most of the MD simulations in this work were carried out on the Dutch national e-infrastructure with the support of SURF Cooperative. Authors IMi, IMa, EL and FB acknowledge support from the Industrial Focus Group XUV Optics of the MESA + Institute for Nanotechnology of the University of Twente; the industrial partners ASML, Carl Zeiss SMT GmbH, and Malvern Panalytical, the Province of Overijssel, and the Netherlands Organisation for Scientific Research (NWO).

The work of IMi, IMa, EL and FB was supported by the Dutch Topconsortia Kennis en Innovatie (TKI) Program on High-Tech Systems and Materials [14 HTSM 05]; The work of VZ and NI was supported by the Russian Science Foundation [Grant No. 19-19-00697]. The work of NM was partially supported by the Czech Ministry of Education, Youth and Sports, Czech Republic [grants numbers LTT17015, LM2015083]. .

Appendix A. Heat conduction with MC pseudo-electrons

We simulate electron heat conduction using the MC approach combined with the classical MD model. The MC model is parameterized with two fitting parameters: the mass of pseudo-electrons (see description in Section 2.3) and the exchange rate determining both the pseudo-electron swapping between neighbouring atoms and pseudo-electron–ion collision rates.

To define the pseudo-electron exchange rate, prior to the main simulations, the problem of heat transfer between two surfaces with different constant temperatures $T_1 > T_2$ is simulated with the MD-MC method. Such a problem has a steady-state solution $T(z) = T_1 - z(T_1 - T_2)/L$, where L is the distance between the two surfaces. Since the solution is time independent, the pseudo-electron mass and pseudo-electron–ion collision rate can be arbitrary. Thus, the required experimental heat flux can be obtained by adjusting the single MC parameter of pseudo-electron exchange rate, which fits the experimental thermal conductivity precisely at the given conditions. As was demonstrated in earlier works, such a method can efficiently treat electronic heat conduction [54].

With the procedure described above we aim to reproduce the experimental thermal conductivity of Ru at the temperature close to the melting point $T_m = 2607$ K. That provides us with an accurate description of the melting and recrystallization front propagation, which is essential in order to obtain the realistic final frozen surface structures in long timescale simulations. The experimental data available in the literature give the value $k_e = 79.6$ W/m/K at $T = 2500$ K [88]. We choose the values for T_1 and T_2 to be 2600 and 2500 K, respectively, and L is 100 nm. The heat flux of $8 \cdot 10^{10}$ W/m^2 for the given temperature gradient can be established by the pseudo-electron exchange rate of 1.8 fs^{-1}.

The pseudo-electron mass m_e^* can be fitted after finding the exchange rate described above. This second MC parameter determines the energy transfer between a pseudo-electron and an atom via their collision governed by the following expressions:

$$\boldsymbol{v}_e' = (m_e^* \boldsymbol{v}_e + m_a \boldsymbol{v}_a + m_a v \boldsymbol{n})/(m_e^* + m_a), \tag{A.1}$$

$$\boldsymbol{v}_a' = (m_e^* \boldsymbol{v}_e + m_a \boldsymbol{v}_a - m_e^* v \boldsymbol{n})/(m_e^* + m_a),$$

where $\boldsymbol{v_e}$, $\boldsymbol{v_a}$ and $\boldsymbol{v_e'}$, $\boldsymbol{v_a'}$ are pseudo-electron and atom velocities in the laboratory system before and after an exchange event, respectively, and v is the pseudo-electron-atom relative speed. The scattering unit vector $\boldsymbol{n}$ is assumed to be distributed isotropically and is provided by a uniform random generator of directions. Such energy exchange conserves the total energy and momentum of the entire pseudo-electron-atom system.

The pseudo-electron mass is obtained within the procedure of linking the 2T-HD code with the MD-MC. The 2T-HD part describes the 2T regime of material evolution, whereas classical MD is only applicable in the 1T regime. For that reason, we link the two parts of our hybrid scheme at the moment of time $\tau = 3$ ps, when the thermal equilibrium between electrons and atoms is reached ($T_e \approx T_i$). The 2T-HD calculations are performed prior to the MD-MC ones to obtain the ion temperature $T_i(z)$ and total pressure $P_{zz}(z)$ depth profiles at $t = \tau$. In the MD-MC code the mass of the pseudo-electrons and the initial heating profile (that mimics the distribution of absorbed laser energy) are adjusted in order to reproduce the $T_i(z)$ and $P_{zz}(z)$ profiles obtained with the 2T-HD (see Fig. 2).

The resulting mass is $m_e^* = 150\, m_e$, where m_e is the free electron mass. Please note that the obtained mass does not have the physical meaning of the effective electron mass, since our MC pseudo-particles should not be considered as real electrons, as explained in Section 2.3. We also remind here that the MC pseudo-electrons provide reliable description of the electron heat conductivity only during the 1T stage. The nonequilibrium electron cascade stage is modeled with the XCASCADE(3D) code, while the electronic system in the 2T regime is accurately described with the 2T-HD equations, where the band structure effects, such as different effective masses of s- and d-electrons are taken into account based on *ab initio* calculations of thermal parameters described in Ref. [64].

Although, technically speaking, with the MD-MC code we obtain results in both time domains, 2T and 1T, the MD-MC code can provide a reliable description of the material evolution only for $t \geqslant \tau$ (see Fig. 1). Thus, from this time onward, the MD code replaces the 2T-HD in our simulation scheme.

Appendix B. Embedded atom model potential for ruthenium

The stress-matching method [66,67] was used to develop an interatomic embedded atom model (EAM) potential for Ru which is capable to reproduce correctly the response of a crystal to compression and stretching in a wide range of strains. The fitting database is built of the stress tensor components $\sigma_{\alpha\beta}(V) = -P_{\alpha\beta}(V)$ calculated with the density functional theory (DFT) method in a cold *hcp* lattice under continuous bulk and uniaxial deformation along the c-axis.

To obtain the first-principles cold pressure curves of Ru and its c/a ratio, DFT calculations were performed using the projector augmented wave (PAW) method [90] with the Vienna *ab initio* simulation package (VASP) [91,92]. The PAW pseudopotential of “sv” type from the standard VASP library, which takes into account two semicore electron bands $4s^2$ and $4p^6$ in addition to the valence electrons, was utilized with the Perdew-Burke-Ernzerhof functional for VASP 5.4, see details and the calculated density of states in [64].

The highly accurate DFT calculations were performed with the energy cutoff of 800 eV and number of k-points $21 \times 21 \times Y$ generated according to the Monkhorst–Pack scheme for sampling the Brillouin zone. Here the number Y takes values from 13 for the maximal ratio $c/a = 2.57$ to $Y = 28$ for the minimal ratio $c/a = 1.18$ in order to keep a constant grid step in the reciprocal space. The number of unoccupied levels was 18 per atom. The *hcp*-lattice cell with two Ru atoms in periodical boundary conditions was used in the DFT calculations. To calculate the uniaxial pressure components, a series of stepwise static calculations were performed for uniaxial strains along the c-axis. Figs. B.15 and B.16 show the obtained DFT data for bulk and c-axis deformations.

The experimental bulk modulus of 310.9 GPa [94], equilibrium density of 12.45 g/cm^3 with the lattice parameters of $c = 0.4273$ nm and $a = 0.27003$ nm [95], and the cohesive energy 6.74 eV [96] of ruthenium were also included in the database. The fitting procedure involves also the ratio c/a as a function of the compression ratio.

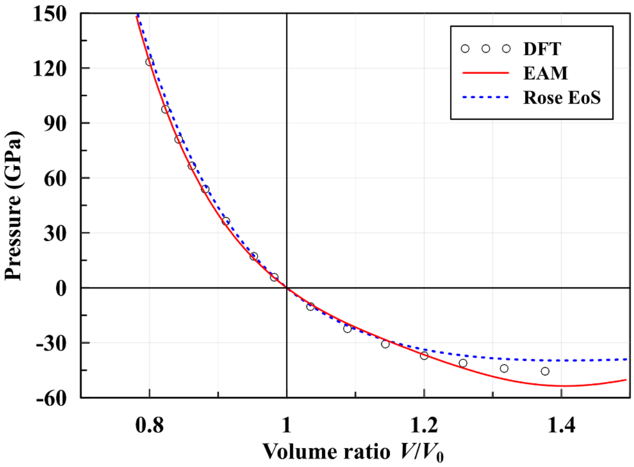

Fig. B.15. Two EAM potentials give almost identical cold pressure curves in bulk compression of Ru. Fitting of the pressure was bounded by $V/V_0 < 1.2$. Dotted line shows $P(V)$ at $T = 0$ K from the universal Rose’s equation of states [89].

The constraints of the monotonic behaviour of $P_{\alpha\alpha}(V)$, including the requirement of an increase of the speed of sound with compression, as well as the absence of solid–solid phase transitions from the stable *hcp* phase of Ru in a wide range of deformation were also applied in the fitting.

The high-order rational functions were used to represent the EAM potential consisting of a pairwise energy, charge density and embedding energy. Fitting of potential coefficients was performed by minimization of a target function with the use of a downhill simplex algorithm combined with a random walk in a multidimensional space of the fitting coefficients [67]. Figs. B.15 and B.16 show the cold pressure curves calculated by our new EAM potential. It shows good agreement with the cold stress–strain curves from DFT in the wide range of deformations, and provides the

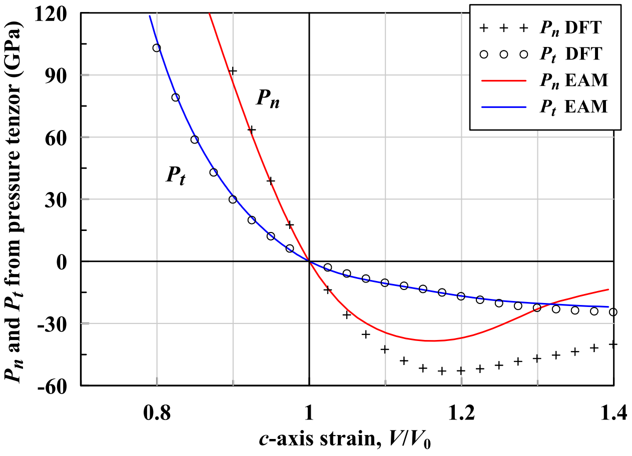

Fig. B.16. Normal P_n and tangential P_t components of the pressure tensor obtained in uniaxial deformation along the c-axis using EAM potential. Fitting was bounded by strains $V/V_0 < 1.1$.

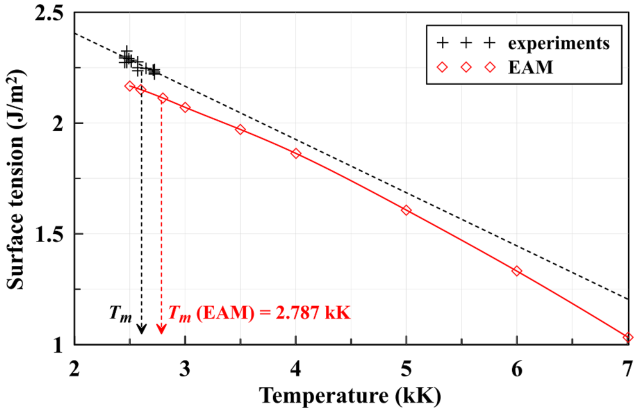

Fig. B.17. Dependence of the Ru surface tension on temperature. Dotted line shows a linear fit of experimental data [93]. Red diamonds show the result of our calculation with the Ru EAM potential.

melting points close to the experimental one T_m = 2607 K, see Fig. B.17.

Fig. B.17 shows the experimental data [93] on the Ru surface tension dependence on temperature in the vicinity of the melting point and a linear extrapolation to higher temperatures. The same dependence is calculated with our EAM potential, demonstrating a good agreement with the experiment.

The obtained EAM potential does not depend on the electron temperature, i.e., a possible influence of the excited electronic system on the interatomic potential is not taken into account. Development of a temperature-dependent potential is challenging [97], and can be considered as a possible future improvement of our model.

Appendix C. Supplementary data

Supplementary data associated with this article can be found, in the online version, at https://doi.org/10.1016/j.apsusc.2020.146952.

References

[1] M. Yabashi, H. Tanaka, T. Ishikawa, Overview of the SACLA facility, J. Synchrotron Radiat. 22 (3) (2015) 477–484, https://doi.org/10.1107/S1600577515004658.

[2] T. Tschentscher, C. Bressler, J. Grünert, A. Madsen, A. Mancuso, M. Meyer, A. Scherz, H. Sinn, U. Zastrau, Photon beam transport and scientific instruments at the European XFEL, Appl. Sci. 7 (6) (2017) 592, https://doi.org/10.3390/app7060592.

[3] F. Graziani, M.P. Desjarlais, R. Redmer, S.B. Trickey, Frontiers and challenges in warm dense matter 96 Springer Science & Business, 2014.

[4] S.P. Hau-Riege, R.A. London, R.M. Bionta, R. Soufli, D. Ryutov, M. Shirk, S.L. Baker, P.M. Smith, P. Nataraj, Multiple pulse thermal damage thresholds of materials for X-ray free electron laser optics investigated with an ultraviolet laser, Appl. Phys. Lett. 93 (20) (2008) 201105, , https://doi.org/10.1063/1.3021081.

[5] J. Pelka, R. Sobierajski, D. Klinger, W. Paszkowicz, J. Krzywinski, M. Jurek, D. Zymierska, A. Wawro, A. Petroutchik, L. Juha, V. Hajkova, J. Cihelka, J. Chalupsky, T. Burian, L. Vysin, S. Toleikis, K. Sokolowski-Tinten, N. Stojanovic, U. Zastrau, R. London, S. Hau-Riege, C. Riekel, R. Davies, M. Burghammer, E. Dynowska, W. Szuszkiewicz, W. Caliebe, R. Nietubyc, Damage in solids irradiated by a single shot of XUV free-electron laser: Irreversible changes investigated using X-ray microdiffraction, atomic force microscopy and Nomarski optical microscopy, Radiat. Phys. Chem. 78 (10) (2009) S46–S52, https://doi.org/10.1016/j.radphyschem.2009.06.006.

[6] A.R. Khorsand, R. Sobierajski, E. Louis, S. Bruijn, E.D. van Hattum, R.W.E. van de Kruijs, M. Jurek, D. Klinger, J.B. Pelka, L. Juha, T. Burian, J. Chalupsky, J. Cihelka, V. Hajkova, L. Vysin, U. Jastrow, N. Stojanovic, S. Toleikis, H. Wabnitz, K. Tiedtke, K. Sokolowski-Tinten, U. Shymanovich, J. Krzywinski, S. Hau-Riege, R. London, A. Gleeson, E.M. Gullikson, F. Bijkerk, Single shot damage mechanism of Mo/Si multilayer optics under intense pulsed XUV-exposure, Opt. Express 18 (2) (2010) 700–712, https://doi.org/10.1364/OE.18.000700.

[7] S. Dastjani Farahani, J. Chalupsky, T. Burian, H. Chapman, A. Gleeson, V. Hajkoya, L. Juha, M. Jurek, D. Klinger, H. Sinn, R. Sobierajski, M. Störmer, K. Tiedtke, S. Toleikis, T. Tschentscher, H. Wabnitz, J. Gaudin, Damage threshold of amorphous carbon mirror for 177 eV FEL radiation, Nucl. Instrum. Meth. A 635 (1) (2011) S39–S42, https://doi.org/10.1016/j.nima.2010.10.133.

[8] A. Aquila, R. Sobierajski, C. Ozkan, V. Hájková, T. Burian, J. Chalupský, L. Juha, M. Störmer, S. Bajt, M.T. Klepka, P. Dłużewski, K. Morawiec, H. Ohashi, T. Koyama, K. Tono, Y. Inubushi, M. Yabashi, H. Sinn, T. Tschentscher, A.P. Mancuso, J. Gaudin, Fluence thresholds for grazing incidence hard X-ray mirrors, Appl. Phys. Lett. 106 (24) (2015) 241905, , https://doi.org/10.1063/1.4922380.

[9] T. Koyama, H. Yumoto, T. Miura, K. Tono, T. Togashi, Y. Inubushi, T. Katayama, J. Kim, S. Matsuyama, M. Yabashi, K. Yamauchi, H. Ohashi, Damage threshold of coating materials on X-ray mirror for X-ray free electron laser, Rev. Sci. Instrum. 87 (5) (2016) 051801, , https://doi.org/10.1063/1.4950723.

[10] R. Sobierajski, I. Jacyna, P. Dłużewski, M.T. Klepka, D. Klinger, J.B. Pełka, T. Burian, V. Hájková, L. Juha, K. Saksl, V. Vozda, I. Makhotkin, E. Louis, B. Faatz, K. Tiedtke, S. Toleikis, H. Enkisch, M. Hermann, S. Strobel, R.A. Loch, J. Chalupsky, Role of heat accumulation in the multi-shot damage of silicon irradiated with femtosecond XUV pulses at a 1 MHz repetition rate, Opt. Express 24 (14) (2016) 15468–15477, https://doi.org/10.1364/OE.24.015468.

[11] I.A. Makhotkin, R. Sobierajski, J. Chalupský, K. Tiedtke, G. de Vries, M. Störmer, F. Scholze, F. Siewert, R.W.E. van de Kruijs, I. Milov, E. Louis, I. Jacyna, M. Jurek, D. Klinger, L. Nittler, Y. Syryanyy, L. Juha, V. Hájková, V. Vozda, T. Burian, K. Saksl, B. Faatz, B. Keitel, E. Plönjes, S. Schreiber, S. Toleikis, R. Loch, M. Hermann, S. Strobel, H.-K. Nienhuys, G. Gwalt, T. Mey, H. Enkisch, Experimental study of EUV mirror radiation damage resistance under long-term free-electron laser exposures below the single-shot damage threshold, J. Synchrotron Radiat. 25 (1) (2018) 77–84, https://doi.org/10.1107/S1600577517017362.

[12] I.A. Makhotkin, I. Milov, J. Chalupský, K. Tiedtke, H. Enkisch, G. de Vries, F. Scholze, F. Siewert, J.M. Sturm, K.V. Nikolaev, R.W.E. van de Kruijs, M.A. Smithers, H.A.G.M. van Wolferen, E.G. Keim, E. Louis, I. Jacyna, M. Jurek, D. Klinger, J.B. Pelka, L. Juha, V. Hájková, V. Vozda, T. Burian, K. Saksl, B. Faatz, B. Keitel, E. Plönjes, S. Schreiber, S. Toleikis, R. Loch, M. Hermann, S. Strobel, R. Donker, T. Mey, R. Sobierajski, Damage accumulation in thin ruthenium films induced by repetitive exposure to femtosecond XUV pulses below the single-shot ablation threshold, J. Opt. Soc. Am. B 35 (11) (2018) 2799–2805, https://doi.org/10.1364/JOSAB.35.002799.

[13] J. Krzywinski, R. Conley, S. Moeller, G. Gwalt, F. Siewert, C. Waberski, T. Zeschke, D. Cocco, Damage thresholds for blaze diffraction gratings and grazing incidence optics at an X-ray free-electron laser, J. Synchrotron Radiat. 25 (1) (2018) 85–90, https://doi.org/10.1107/S1600577517016083.

[14] R. Follath, T. Koyama, V. Lipp, N. Medvedev, K. Tono, H. Ohashi, L. Patthey, M. Yabashi, B. Ziaja, X-ray induced damage of B4C-coated bilayer materials under various irradiation conditions, Sci. Rep. 9 (1) (2019) 2029, https://doi.org/10.1038/s41598-019-38556-0.

[15] B.N. Chichkov, C. Momma, S. Nolte, F. Von Alvensleben, A. Tünnermann, Femtosecond, picosecond and nanosecond laser ablation of solids, Appl. Phys. A 63 (2) (1996) 109–115, https://doi.org/10.1007/BF01567637.

[16] R. Ernstorfer, M. Harb, C.T. Hebeisen, G. Sciaini, T. Dartigalongue, R.D. Miller, The formation of warm dense matter: experimental evidence for electronic bond hardening in gold, Science 323 (5917) (2009) 1033–1037, https://doi.org/10.1126/science.1162697.

[17] E. García Saiz, G. Gregori, D.O. Gericke, J. Vorberger, B. Barbrel, R.J. Clarke, R.R. Freeman, S.H. Glenzer, F.Y. Khattak, M. Koenig, O.L. Landen, D. Neely, P. Neumayer, M.M. Notley, A. Pelka, D. Price, M. Roth, M. Schollmeier, C. Spindloe, R.L. Weber, L. van Woerkom, K. Wünsch, D. Riley, Probing warm dense lithium by inelastic X-ray scattering, Nat. Phys. 4 (12) (2008) 940, https://doi.org/10.1038/nphys1103.

[18] N. Medvedev, B. Ziaja, Multistep transition of diamond to warm dense matter state revealed by femtosecond X-ray diffraction, Sci. Rep. 8 (1) (2018) 5284, https://doi.org/10.1038/s41598-018-23632-8.

[19] M.N. Ashfold, F. Claeyssens, G.M. Fuge, S.J. Henley, Pulsed laser ablation and deposition of thin films, Chem. Soc. Rev. 33 (1) (2004) 23–31, https://doi.org/10.1039/B207644F.

[20] T.A. Labutin, V.N. Lednev, A.A. Ilyin, A.M. Popov, Femtosecond laser-induced breakdown spectroscopy, J. Anal. At. Spectrom. 31 (1) (2016) 90–118, https://doi.org/10.1039/C5JA00301F.

[21] C. Phipps, C. Bonnal, F. Masson, P. Musumeci, Launching swarms of microsatellites using a 100 kW average power pulsed laser, J. Opt. Soc. Am. B 35 (10) (2018) B20–B26, https://doi.org/10.1364/JOSAB.35.000B20.

[22] L. Koch, S. Kuhn, H. Sorg, M. Gruene, S. Schlie, R. Gaebel, B. Polchow, K. Reimers, S. Stoelting, N. Ma, P.M. Vogt, G. Steinhoff, B. Chichkov, Laser printing of skin cells and human stem cells, Tissue Eng. Part C Methods 16 (5) (2009) 847–854, https://doi.org/10.1089/ten.tec.2009.0397.

[23] R.R. Gattass, E. Mazur, Femtosecond laser micromachining in transparent materials, Nat. Photonics 2 (4) (2008) 219, https://doi.org/10.1038/nphoton.2008.47.

[24] H. Zeng, X.-W. Du, S.C. Singh, S.A. Kulinich, S. Yang, J. He, W. Cai, Nanomaterials via laser ablation/irradiation in liquid: a review, Adv. Funct. Mater. 22 (7) (2012) 1333–1353, https://doi.org/10.1002/adfm.201102295.

[25] E. Messina, E. Cavallaro, A. Cacciola, M.A. Iatì, P.G. Gucciardi, F. Borghese, P. Denti, R. Saija, G. Compagnini, M. Meneghetti, V. Amendola, O.M. Maragò, Plasmon-enhanced optical trapping of gold nanoaggregates with selected optical properties, ACS Nano 5 (2) (2011) 905–913, https://doi.org/10.1021/nn102101a.

[26] The effect of the Au loading on the liquid-phase aerobic oxidation of ethanol over Au/TiO2 catalysts prepared by pulsed laser ablation, J. Catal. 330 (2015) 497 – 506. doi: https://doi.org/10.1016/j.jcat.2015.07.033.

[27] T. Baati, A. Al-Kattan, M.-A. Esteve, L. Njim, Y. Ryabchikov, F. Chaspoul, M. Hammami, M. Sentis, A.V. Kabashin, D. Braguer, Ultrapure laser-synthesized Si-based nanomaterials for biomedical applications: in vivo assessment of safety and biodistribution, Sci. Rep. 6 (2016) 25400, https://doi.org/10.1038/srep25400.

[28] K. Nordlund, C. Björkas, T. Ahlgren, A. Lasa, A.E. Sand, Multiscale modelling of plasma-wall interactions in fusion reactor conditions, J. Phys. D: Appl. Phys. (22) (2014) 224018, https://doi.org/10.1088/0022-3727/47/22/224018.

[29] Y. Rong, P. Ji, M. He, Y. Zhang, Y. Tang, Multiscale investigation of femtosecond laser pulses processing aluminum in burst mode, Nanosc. Microsc. Therm. 22 (4) (2018) 324–347, https://doi.org/10.1080/15567265.2018.1497111.

[30] N. Medvedev, V. Tkachenko, V. Lipp, Z. Li, B. Ziaja, Various damage mechanisms in carbon and silicon materials under femtosecond X-ray irradiation, 4open 1 (2018) 3, https://doi.org/10.1051/fopen/2018003.

[31] M. Kaganov, I. Lifshitz, L. Tanatarov, Relaxation between electrons and crystalline lattice, Sov. Phys. JETP 4 (2) (1957) 173.

[32] S. Anisimov, A. Bonch-Bruevich, M. El'yashevich, Y. Imas, N. Pavlenko, G. Romanov, Effect of powerful light (laser) fluxes on metals, Zh. Tekh. Fiz 36 (1967) 1273.

[33] S. Anisimov, B. Kapeliovich, T. Perelman, Electron emission from metal surfaces exposed to ultrashort laser pulses, Zh. Eksp. Teor. Fiz 66 (2) (1974) 776.

[34] S. Anisimov, N. Inogamov, Y.V. Petrov, V. Khokhlov, V. Zhakhovskii, K. Nishihara, M. Agranat, S. Ashitkov, P. Komarov, Interaction of short laser pulses with metals at moderate intensities, Appl. Phys. A 92 (4) (2008) 939–943, https://doi.org/10.1007/s00339-008-4607-y.

[35] D.S. Ivanov, L.V. Zhigilei, Combined atomistic-continuum modeling of short-pulse laser melting and disintegration of metal films, Phys. Rev. B 68 (2003) 064114, , https://doi.org/10.1103/PhysRevB.68.064114.

[36] B.J. Demaske, V.V. Zhakhovsky, N.A. Inogamov, I.I. Oleynik, Ablation and spallation of gold films irradiated by ultrashort laser pulses, Phys. Rev. B 82 (6) (2010) 064113, , https://doi.org/10.1103/PhysRevB.82.064113.

[37] S.V. Starikov, V.V. Pisarev, Atomistic simulation of laser-pulse surface modification: predictions of models with various length and time scales, J. Appl. Phys. 117 (13) (2015) 135901, , https://doi.org/10.1063/1.4916600.

[38] N.A. Inogamov, V.V. Zhakhovsky, V.A. Khokhlov, Y.V. Petrov, K.P. Migdal, Solitary nanostructures produced by ultrashort laser pulse, Nanoscale Res. Lett. 11 (1) (2016) 177, https://doi.org/10.1186/s11671-016-1381-1.

[39] H.M. van Driel, Kinetics of high-density plasmas generated in Si by 1.06- and 0.53-μm picosecond laser pulses, Phys. Rev. B 35 (1987) 8166–8176, https://doi.org/10.1103/PhysRevB.35.8166.

[40] J. Chen, D. Tzou, J. Beraun, Numerical investigation of ultrashort laser damage in semiconductors, Int. J. Heat Mass Trans. 48 (3–4) (2005) 501–509, https://doi.org/10.1016/j.ijheatmasstransfer.2004.09.015.

[41] Y. Gan, J. Chen, Combined continuum-atomistic modeling of ultrashort-pulsed laser irradiation of silicon, Appl. Phys. A 105 (2) (2011) 427–437, https://doi.org/10.1007/s00339-011-6573-z.

[42] V.P. Lipp, B. Rethfeld, M.E. Garcia, D.S. Ivanov, Atomistic-continuum modeling of short laser pulse melting of Si targets, Phys. Rev. B 90 (2014) 245306, , https://doi.org/10.1103/PhysRevB.90.245306.

[43] P. Lorazo, L.J. Lewis, M. Meunier, Thermodynamic pathways to melting, ablation, and solidification in absorbing solids under pulsed laser irradiation, Phys. Rev. B 73 (2006) 134108, , https://doi.org/10.1103/PhysRevB.73.134108.

[44] W.S. Fann, R. Storz, H.W.K. Tom, J. Bokor, Electron thermalization in gold, Phys. Rev. B 46 (1992) 13592–13595, https://doi.org/10.1103/PhysRevB.46.13592.

[45] C.-K. Sun, F. Vallée, L.H. Acioli, E.P. Ippen, J.G. Fujimoto, Femtosecond-tunable measurement of electron thermalization in gold, Phys. Rev. B 50 (1994) 15337–15348, https://doi.org/10.1103/PhysRevB.50.15337.

[46] D. Bejan, G. Raseev, Nonequilibrium electron distribution in metals, Phys. Rev. B 55 (1997) 4250–4256, https://doi.org/10.1103/PhysRevB.55.4250.

[47] A.V. Lugovskoy, I. Bray, Ultrafast electron dynamics in metals under laser irradiation, Phys. Rev. B 60 (1999) 3279–3288, https://doi.org/10.1103/PhysRevB.60.3279.

[48] B. Rethfeld, A. Kaiser, M. Vicanek, G. Simon, Ultrafast dynamics of nonequilibrium electrons in metals under femtosecond laser irradiation, Phys. Rev. B 65 (21) (2002) 214303, , https://doi.org/10.1103/PhysRevB.65.214303.

[49] J. Sempau, E. Acosta, J. Baro, J. Fernández-Varea, F. Salvat, An algorithm for Monte Carlo simulation of coupled electron-photon transport, Nucl. Instrum. Meth. B 132 (3) (1997) 377–390, https://doi.org/10.1016/S0168-583X(97)00414-X.

[50] N. Medvedev, Femtosecond X-ray induced electron kinetics in dielectrics: application for FEL-pulse-duration monitor, Appl. Phys. B 118 (3) (2015) 417–429, https://doi.org/10.1007/s00340-015-6005-4.

[51] V. Lipp, N. Medvedev, B. Ziaja, Classical Monte-Carlo simulations of X-ray induced electron cascades in various materials, Proc. SPIE 10236 (2017) 102360H, https://doi.org/10.1117/12.2267939.

[52] O. Peyrusse, J.-M. André, P. Jonnard, J. Gaudin, Modeling of the interaction of an X-ray free-electron laser with large finite samples, Phys. Rev. E 96 (4) (2017) 043205, , https://doi.org/10.1103/PhysRevE.96.043205.

[53] I. Milov, V. Lipp, D. Ilnitsky, N. Medvedev, K. Migdal, V. Zhakhovsky, V. Khokhlov, Y. Petrov, N. Inogamov, S. Semin, et al., Similarity in ruthenium damage induced by photons with different energies: From visible light to hard X-rays, Appl. Surf. Sci. 501 (2020) 143973, , https://doi.org/10.1016/j.apsusc.2019.143973.

[54] V. Zhakhovskii, K. Nishihara, Y. Fukuda, S. Shimojo, T. Akiyama, S. Miyanaga, H. Sone, H. Kobayashi, E. Ito, Y. Seo, M. Tamura, Y. Ueshima, A new dynamical domain decomposition method for parallel molecular dynamics simulation, IEEE International Symposium on Cluster Computing and the Grid 2 (2005) 848–854, https://doi.org/10.1109/CCGRID.2005.1558650.

[55] M. Egorova, S. Dyachkov, A. Parshikov, V. Zhakhovsky, Parallel SPH modeling using dynamic domain decomposition and load balancing displacement of voronoi subdomains, Comput. Phys. Commun. 234 (2019) 112–125, https://doi.org/10.1016/j.cpc.2018.07.019.

[56] W. Ackermann, G. Asova, V. Ayvazyan, A. Azima, N. Baboi, J. Bähr, V. Balandin, B. Beutner, A. Brandt, A. Bolzmann, R. Brinkmann, O.I. Brovko, M. Castellano, P. Castro, L. Catani, E. Chiadroni, S. Choroba, A. Cianchi, J.T. Costello, D. Cubaynes, J. Dardis, W. Decking, H. Delsim-Hashemi, A. Delserieys, G. Di Pirro, M. Dohlus, S. Düsterer, A. Eckhardt, H.T. Edwards, B. Faatz, J. Feldhaus, K. Flöttmann, J. Frisch, L. Fröhlich, T. Garvey, U. Gensch, C. Gerth, M. Görler, N. Golubeva, H.-J. Grabosch, M. Grecki, O. Grimm, K. Hacker, U. Hahn, J.H. Han, K. Honkavaara, T. Hott, M. Hüning, Y. Ivanisenko, E. Jaeschke, W. Jalmuzna, T. Jezynski, R. Kammering, V. Katalev, K. Kavanagh, E.T. Kennedy, S. Khodyachykh, K. Klose, V. Kocharyan, M. Körfer, M. Kollewe, W. Koprek, S. Korepanov, D. Kostin, M. Krassilnikov, G. Kube, M. Kuhlmann, C.L.S. Lewis, L. Lilje, T. Limberg, D. Lipka, F. Löhl, H. Luna, M. Luong, M. Martins, M. Meyer, P. Michelato, V. Miltchev, W.D. Möller, L. Monaco, W.F.O. Müller, O. Napieralski, O. Napoly, P. Nicolosi, D. Nölle, T. Nuñez, A. Oppelt, C. Pagani, R. Paparella, N. Pchalek, J. Pedregosa-Gutierrez, B. Petersen, B. Petrosyan, G. Petrosyan, L. Petrosyan, J. Pflüger, E. Plönjes, L. Poletto, K. Pozniak, E. Prat, D. Proch, P. Pucyk, P. Radcliffe, H. Redlin, K. Rehlich, M. Richter, M. Roehrs, J. Roensch, R. Romaniuk, M. Ross, J. Rossbach, V. Rybnikov, M. Sachwitz, E.L. Saldin, W. Sandner, H. Schlarb, B. Schmidt, M. Schmitz, P. Schmüser, J.R. Schneider, E.A. Schneidmiller, S. Schnepp, S. Schreiber, M. Seidel, D. Sertore, A.V. Shabunov, C. Simon, S. Simrock, E. Sombrowski, A.A. Sorokin, P. Spanknebel, R. Spesyvtsev, L. Staykov, B. Steffen, F. Stephan, F. Stulle, H. Thom, K. Tiedtke, M. Tischer, S. Toleikis, R. Treusch, D. Trines, I. Tsakov, E. Vogel, T. Weiland, H. Weise, M. Wellhöfer, M. Wendt, I. Will, A. Winter, K. Wittenburg, W. Wurth, P. Yeates, M.V. Yurkov, I. Zagorodnov, K. Zapfe, Operation of a free-electron laser from the extreme ultraviolet to the water window, Nat. Photonics 1 (6) (2007) 336–342, https://doi.org/10.1038/nphoton.2007.76.

[57] I. Milov, I.A. Makhotkin, R. Sobierajski, N. Medvedev, V. Lipp, J. Chalupský, J.M. Sturm, K. Tiedtke, G. de Vries, M. Störmer, F. Siewert, R. van de Kruijs, E. Louis, I. Jacyna, M. Jurek, L. Juha, V. Hájková, V. Vozda, T. Burian, K. Saksl, B. Faatz, B. Keitel, E. Plönjes, S. Schreiber, S. Toleikis, R. Loch, M. Hermann, S. Strobel, H.-K. Nienhuys, G. Gwalt, T. Mey, H. Enkisch, F. Bijkerk, Mechanism of single-shot damage of Ru thin films irradiated by femtosecond extreme UV free-electron laser, Opt. Express 26 (15) (2018) 19665, https://doi.org/10.1364/OE.26.019665.

[58] B. Rethfeld, D.S. Ivanov, M.E. Garcia, S.I. Anisimov, Modelling ultrafast laser ablation, J. Phys. D Appl. Phys. 50 (19) (2017) 193001, , https://doi.org/10.1088/1361-6463/50/19/193001.

[59] L.V. Zhigilei, Z. Lin, D.S. Ivanov, Atomistic modeling of short pulse laser ablation of metals: connections between melting, spallation, and phase explosion, J. Phys. Chem. C 113 (27) (2009) 11892–11906, https://doi.org/10.1021/jp902294m.

[60] N.M. Bulgakova, R. Stoian, A. Rosenfeld, I. Hertel, W. Marine, E. Campbell, A general continuum approach to describe fast electronic transport in pulsed laser irradiated materials: the problem of Coulomb explosion, Appl. Phys. A 81 (2) (2005) 345–356, https://doi.org/10.1007/s00339-005-3242-0.

[61] D. Cullen, A survey of atomic binding energies for use in EPICS2017, Tech. rep., Vienna (2018).

[62] D.A. Chapman, D.O. Gericke, Analysis of Thomson scattering from nonequilibrium plasmas, Phys. Rev. Lett. 107 (2011) 165004, , https://doi.org/10.1103/PhysRevLett.107.165004.

[63] N. Medvedev, A. Volkov, B. Ziaja, Electronic and atomic kinetics in solids irradiated with free-electron lasers or swift-heavy ions, Nucl. Instrum. Meth. B 365 (2015) 437–446, https://doi.org/10.1016/j.nimb.2015.08.063.

[64] Y. Petrov, K. Migdal, N. Inogamov, V. Khokhlov, D. Ilnitsky, I. Milov, N. Medvedev, V. Lipp, V. Zhakhovsky, Ruthenium under ultrafast laser excitation: Model and

dataset for equation of state, conductivity, and electron-ion coupling, Data in Brief 28 (2020) 104980, , https://doi.org/10.1016/j.dib.2019.104980.

[65] N.A. Inogamov, V.V. Zhakhovsky, Surface 3D nanostructuring by tightly focused laser pulse: simulations by Lagrangian code and molecular dynamics, J. Phys. Conf. Ser. 681 (1) (2016) 012001, , https://doi.org/10.1088/1742-6596/681/1/012001.

[66] V. Zhakhovskii, N. Inogamov, Y. Petrov, S. Ashitkov, K. Nishihara, Molecular dynamics simulation of femtosecond ablation and spallation with different interatomic potentials, Appl. Surf. Sci. 255 (24) (2009) 9592–9596, https://doi.org/10.1016/j.apsusc.2009.04.082.

[67] V.V. Zhakhovsky, K.P. Migdal, N.A. Inogamov, S.I. Anisimov, MD simulation of steady shock-wave fronts with phase transition in single-crystal iron, in: AIP Conf. Proc., no. January, p. 070003. doi:10.1063/1.4971591.

[68] B.J. Demaske, V.V. Zhakhovsky, N.A. Inogamov, I.I. Oleynik, Ultrashort shock waves in nickel induced by femtosecond laser pulses, Phys. Rev. B 87 (5) (2013) 054109, , https://doi.org/10.1103/PhysRevB.87.054109.

[69] I. Milov, V. Lipp, N. Medvedev, I.A. Makhotkin, E. Louis, F. Bijkerk, Modeling of XUV-induced damage in Ru films: the role of model parameters, J. Opt. Soc. Am. B 35 (10) (2018) B43–B53, https://doi.org/10.1364/JOSAB.35.000B43.

[70] A.E. Morris, H.A. Fine, G. Geiger, Handbook on Material and Energy Balance Calculations in Material Processing, Includes CD-ROM, John Wiley Sons, 2011.

[71] B. Keene, Review of data for the surface tension of pure metals, Int. Mater. Rev. 38 (4) (1993) 157–192, https://doi.org/10.1179/imr.1993.38.4.157.

[72] V.P. Skripov, Metastable Liquids, Wiley, New York, 1974.

[73] M.M. Basko, M.S. Krivokorytov, A.Y. Vinokhodov, Y.V. Sidelnikov, V.M. Krivtsun, V.V. Medvedev, D.A. Kim, V.O. Kompanets, A.A. Lash, K.N. Koshelev, Fragmentation dynamics of liquid-metal droplets under ultra-short laser pulses, Laser Phys. Lett. 14 (3) (2017) 036001, https://doi.org/10.1088/1612-202X/aa539b.

[74] N.A. Inogamov, V.V. Zhakhovskii, V.A. Khokhlov, Dynamics of gold ablation into water, JETP 127 (1) (2018) 79–106, https://doi.org/10.1134/S1063776118070075.

[75] K.O. Mikaelian, Rayleigh-taylor instability in finite-thickness fluids with viscosity and surface tension, Phys. Rev. E 54 (4) (1996) 3676, https://doi.org/10.1103/PhysRevE.54.3676.

[76] J.M. Liu, Simple technique for measurements of pulsed Gaussian-beam spot sizes, Opt. Lett. 7 (5) (1982) 196, https://doi.org/10.1364/OL.7.000196.

[77] J.-M. Savolainen, M.S. Christensen, P. Balling, Material swelling as the first step in the ablation of metals by ultrashort laser pulses, Phys. Rev. B 84 (2011) 193410, , https://doi.org/10.1103/PhysRevB.84.193410.

[78] S.I. Ashitkov, N. Inogamov, V.V. Zhakhovskii, Y.N. Emirov, M.B. Agranat, I. Oleinik, S.I. Anisimov, V.E. Fortov, Formation of nanocavities in the surface layer of an aluminum target irradiated by a femtosecond laser pulse, JETP Lett. 95 (4) (2012) 176–181, https://doi.org/10.1134/S0021364012040042.

[79] C. Wu, M.S. Christensen, J.-M. Savolainen, P. Balling, L.V. Zhigilei, Generation of subsurface voids and a nanocrystalline surface layer in femtosecond laser irradiation of a single-crystal Ag target, Phys. Rev. B 91 (3) (2015) 035413, , https://doi.org/10.1103/PhysRevB.91.035413.

[80] Z. Lin, L.V. Zhigilei, V. Celli, Electron-phonon coupling and electron heat capacity of metals under conditions of strong electron-phonon nonequilibrium, Phys. Rev. B 77 (7) (2008) 075133, , https://doi.org/10.1103/PhysRevB.77.075133.

[81] C. Wu, L.V. Zhigilei, Microscopic mechanisms of laser spallation and ablation of metal targets from large-scale molecular dynamics simulations, Appl. Phys. A 114 (1) (2014) 11–32, https://doi.org/10.1007/s00339-013-8086-4.

[82] C.-Y. Shih, M.V. Shugaev, C. Wu, L.V. Zhigilei, Generation of subsurface voids, incubation effect, and formation of nanoparticles in short pulse laser interactions with bulk metal targets in liquid: Molecular dynamics study, J. Phys. Chem. C 121 (30) (2017) 16549–16567, https://doi.org/10.1021/acs.jpcc.7b02301.

[83] K. Sokolowski-Tinten, J. Bialkowski, A. Cavalleri, D. von der Linde, A. Oparin, J. Meyer-ter Vehn, S. Anisimov, Transient states of matter during short pulse laser ablation, Phys. Rev. Lett. 81 (1) (1998) 224, https://doi.org/10.1103/PhysRevLett.81.224.

[84] N. Inogamov, Y.V. Petrov, S. Anisimov, A. Oparin, N. Shaposhnikov, D. Von der Linde, I. Meyer-ter Vehn, Expansion of matter heated by an ultrashort laser pulse, JETP Lett. 69 (4) (1999) 310–316, https://doi.org/10.1134/1.568029.

[85] K.J. Schrider, B. Torralva, S.M. Yalisove, The dynamics of femtosecond pulsed laser removal of 20 nm Ni films from an interface, Appl. Phys. Lett. 107 (12) (2015) 124101, , https://doi.org/10.1063/1.4930939.

[86] M. Nishikino, N. Hasegawa, T. Tomita, Y. Minami, T. Eyama, N. Kakimoto, R. Izutsu, M. Baba, T. Kawachi, T. Suemoto, Formation of X-ray newton's rings from nano-scale spallation shells of metals in laser ablation, AIP Adv. 7 (1) (2017) 015311, , https://doi.org/10.1063/1.4975218.

[87] C.M. Rouleau, C.-Y. Shih, C. Wu, L.V. Zhigilei, A.A. Puretzky, D.B. Geohegan, Nanoparticle generation and transport resulting from femtosecond laser ablation of ultrathin metal films: time-resolved measurements and molecular dynamics simulations, Appl. Phys. Lett. 104 (19) (2014) 193106, , https://doi.org/10.1063/1.4876601.

[88] C.Y. Ho, R.W. Powell, P.E. Liley, Thermal conductivity of the elements, J. Phys. Chem. Ref. Data 1 (2) (1972) 279–421, https://doi.org/10.1063/1.3253100.

[89] J.H. Rose, J.R. Smith, F. Guinea, J. Ferrante, Universal features of the equation of state of metals, Phys. Rev. B 29 (1984) 2963–2969, https://doi.org/10.1103/PhysRevB.29.2963.

[90] P.E. Blöchl, Projector augmented-wave method, Phys. Rev. B 50 (24) (1994) 17953, https://doi.org/10.1103/PhysRevB.50.17953.

[91] G. Kresse, J. Hafner, Ab initio molecular dynamics for liquid metals, Phys. Rev. B. 47 (1) (1993) 558, https://doi.org/10.1103/PhysRevB.47.558.

[92] G. Kresse, J. Furthmüller, Efficient iterative schemes for ab initio total-energy calculations using a plane-wave basis set, Phys. Rev. B 54 (16) (1996) 11169, https://doi.org/10.1103/PhysRevB.54.11169.

[93] P. Paradis, T. Ishikawa, S. Yoda, Thermophysical properties of liquid and supercooled ruthenium measured by noncontact methods, J. Mater. Res. 19 (2) (2004) 590–594, https://doi.org/10.1557/jmr.2004.19.2.590.

[94] R.O. Simmons, H. Wang, Single Crystal Elastic Constants and Calculated Aggregate Properties: A Handbook, MIT Press, Cambridge, 1991.

[95] W.B. Pearson, Handbook of Lattice Spacings and Structure of Metals and Alloys, Pergamon, Oxford, 1967.

[96] C. Kittel, Introduction to Solid State Physics, eighth ed., John Wiley & Sons Inc, 2005.

[97] B. Bauerhenne, V.P. Lipp, T. Zier, E.S. Zijlstra, M.E. Garcia, Self-learning method for construction of analytical interatomic potentials to describe laser-excited materials, Phys. Rev. Lett. 124 (8) (2020) 085501, , https://doi.org/10.1103/PhysRevLett.124.085501.